

THESIS

THE IMPACTS OF AMAZON DEFORESTATION ON PACIFIC CLIMATE

Submitted by

Leah Lindsey

Department of Atmospheric Science

In partial fulfillment of the requirements

For the Degree of Master of Science

Colorado State University

Fort Collins, Colorado

Fall 2016

Master's Committee:

Advisor: David A. Randall

A. Scott Denning
Allan T. Kirkpatrick

Copyright by Leah Lindsey 2016

All Rights Reserved

ABSTRACT

THE IMPACTS OF AMAZON DEFORESTATION ON PACIFIC CLIMATE

Variability in eastern Pacific sea surface temperatures (SSTs) associated with the El Niño Southern Oscillation are known to affect Amazonian precipitation, but to what extent do changing Amazonian vegetation and rainfall impact eastern Pacific SST? The Amazon rainforest is threatened by many factors including climate change and clearing for agricultural reasons. Forest fires and dieback are more likely due to increased frequency and intensity of droughts in the region. It is possible that extensive Amazon deforestation can enhance El Niño conditions by weakening the Walker circulation.

Correlations between annual rainfall rates over the Amazon and other atmospheric parameters (global precipitation, surface air temperature, low cloud amount, 500 hPa vertical velocity, surface winds, and 200 hPa winds) over the eastern Pacific indicate strong relationships among these fields. Maps of these correlations (teleconnection maps) reveal that when the Amazon is rainy, SSTs in the central and eastern Pacific are cold, rainfall is suppressed over the central and eastern Pacific, low clouds are prominent over the eastern and southeastern Pacific, and subsidence over the central and eastern Pacific is enhanced. Precipitation in the Amazon is also consistent with a strong Walker circulation (La Niña conditions), manifest as strong correlations with the easterly surface and westerly 200 hPa zonal winds. Coupling between Amazon rainfall and these fields are seen in observations and model data. Correlations were calculated using data from observations, reanalysis data, two models under the Coupled Model Intercomparison Project/Atmospheric Model Intercomparison Project (CMIP5/AMIP), and an AMIP run with the model used in this study, the

Community Earth System Model (CESM1.1.1). Although the correlations between Amazon precipitation and the aforementioned fields are strong, they do not show causality. In order to investigate the impact of tropical South American deforestation on the Pacific climate, numerical experiments were performed using the CESM.

Amazon deforestation was studied in an idealized world where a single continent was covered in forest and then, in a separate simulation, covered in grassland. Four different sets of simulations were carried out: 1) the baseline idealized set-up with prescribed SST, 2) another with an Andes-like mountain range, 3) a simulation with a slab ocean model rather than prescribed SST, and 4) a simulation repeated with the standard Community Atmosphere Model (CAM4) replaced by the Superparameterized version (SP-CAM). The continent in these simulations was compared to the Amazon, and the ocean to the west of the continent was compared to the eastern Pacific.

All of the simulations showed a strong warming of around 3-4°C over the continent going from forest to grassland. A notable decrease in precipitation over land of about 1-3 mm day⁻¹ and increase to the west of the continent of about 1-2 mm day⁻¹ was also observed in most of the simulations. The simulations with the slab ocean model showed enhanced precipitation changes with a corresponding decrease of 2-4 mm day⁻¹ over land and increase of 3-5 mm day⁻¹ west of the continent. Simulations which used the SP-CAM showed very small changes in precipitation, which was likely due to the decreased spin-up time allowed for these simulations. The decrease in the surface roughness and reduction in the evapotranspiration for the simulations with grassland contributed to these changes in surface temperature and precipitation. The conversion of forest to grassland in our experiments imply that deforestation can lead to weakening of the Walker circulation by weakening easterly

surface winds and westerly upper tropospheric winds. These findings suggest that large-scale Amazon deforestation is capable of enhancing El Niño conditions.

ACKNOWLEDGEMENTS

I would like to thank my advisor, David Randall, for his guidance, support, and patience during my time here at CSU; to the rest of my committee, Scott Denning and Allan Kirkpatrick, for their time and input; to Mark Branson for helping me run and make modifications to the model; to Kelley Wittmeyer and Mostafa Elkady for technical support; to Mark Branson and Ian Baker for helpful discussions along the way; to the rest of the Randall group and folks at CMMAP; and finally to my friends and family for their support throughout this process.

This thesis is typeset in \LaTeX using a document class designed by Leif Anderson.

TABLE OF CONTENTS

Abstract	ii
Acknowledgements	iv
List of Tables	vii
List of Figures	viii
Chapter 1. Introduction and Background	1
1.1. The Walker Circulation	2
1.2. Interannual Variability in the Tropical Pacific	4
1.3. SST Impacts on Tropical South American Precipitation	7
1.4. Amazon Drought, Deforestation, and Climate Change	10
1.5. Outline	16
Chapter 2. Teleconnections	17
2.1. Observations	17
2.1.1. Data	17
2.1.1.1. GPCP and GPCC Precipitation Data	17
2.1.1.2. ISCCP Low Clouds	19
2.1.1.3. ERA Interim Reanalysis	19
2.1.2. Results	20
2.2. AMIP & CMIP5 Data	23
2.2.1. Models and Data	23
2.2.2. Results	24
2.3. CESM AMIP Simulation	27

2.3.1. Model Description.....	27
2.3.2. Results.....	28
2.4. Discussion.....	28
Chapter 3. Model and Experimental Design.....	31
3.1. Model Description.....	31
3.2. Idealized Simulations.....	31
3.2.1. Baseline Simulations.....	31
3.2.2. Simulations with Topography.....	34
3.2.3. Simulations with a Slab Ocean Model.....	35
3.2.4. Simulations with SP-CAM.....	35
Chapter 4. Results of Idealized Simulations.....	37
4.1. Baseline Simulations.....	37
4.2. Simulations with Topography.....	46
4.3. Simulations with a Slab Ocean Model.....	49
4.4. Simulations with SP-CAM.....	51
Chapter 5. Conclusions.....	56
5.1. Summary and Discussion.....	56
5.1.1. Conventional CAM Simulations.....	56
5.1.2. SP-CAM Simulations.....	59
5.2. Future Work.....	60
REFERENCES.....	62

LIST OF TABLES

3.1	Surface characteristics for FOREST and GRASSLAND simulations.....	33
3.2	Summary of numerical experiments with CESM.....	36

LIST OF FIGURES

1.1	Schematic of Walker circulation.	2
1.2	Schematic of Walker circulation during El Niño conditions.	5
1.3	Correlation between SST anomalies in ENSO region and global SST.	7
1.4	Spearman’s rank correlation between the Niño 3.4 index and global precipitation.	10
2.1	Time series of ISCCP low cloud amount.	18
2.2	Teleconnection maps using observational data.	21
2.3	Teleconnection maps using CCSM4-CMIP5 data.	25
2.4	Teleconnection maps using MIROC5-CMIP5 data.	26
2.5	Teleconnections maps using AMIP CESM simulations.	29
2.6	Monthly mean Amazon precipitation.	30
3.1	(a) Land cover and (b) SST distribution for idealized simulations.	32
3.2	Surface geopotential of idealized topography in FOREST_TOPO and GRASSLAND_TOPO simulations.	34
4.1	FOREST, GRASSLAND, and GRASSLAND-FOREST surface temperature (a, c, e) and precipitation rates (b, d, f).	39
4.2	FOREST, GRASSLAND, and GRASSLAND-FOREST low cloud amount (a, c, e) and 500 hPa vertical velocity (b, d, f).	41
4.3	FOREST, GRASSLAND, and GRASSLAND-FOREST surface zonal wind (a, c, e) and 200 hPa zonal wind (b, d, f). For the difference plots, the contours show the change in direction of the zonal wind.	43

4.4	FOREST, GRASSLAND and GRASSLAND-FOREST net surface energy balance (a, c, e) and surface latent heat flux (b, d, f).	45
4.5	Difference plots (GRASSLAND_TOPO-FOREST_TOPO) for (a) surface temperature (b) precipitation rate, (c) low cloud amount, and (d) 500 hPa vertical velocity.	47
4.6	Difference plots (GRASSLAND_TOPO-FOREST_TOPO) for (a) surface zonal wind (b) 200 hPa zonal wind, (c) net surface energy flux, and (d) surface latent heat flux.	48
4.7	Difference plots (GRASSLAND_SOM-FORSET_SOM) for simulations with slab ocean model for (a) surface temperature, (b) precipitation rate, (c) low cloud amount, (d) 500 hPa vertical velocity, (e) surface zonal wind, and (f) 200 hPa zonal wind.	52
4.8	Difference plots (GRASSLAND_SP-FOREST_SP) for (a) surface temperature (b) precipitation rate, (c) low cloud amount, and (d) 500 hPa vertical velocity. . . .	53
4.9	Diurnal cycle of precipitation in simulations for basic set-up and SP-CAM runs. . .	53
4.10	Difference plots (GRASSLAND_SP-FOREST_SP) for (a) surface zonal wind (b) 200 hPa zonal wind, (c) net surface energy flux, and (d) surface latent heat flux. .	55
5.1	Schematic of circulation in simulations with (a) forest and (b) grassland.	58

CHAPTER 1

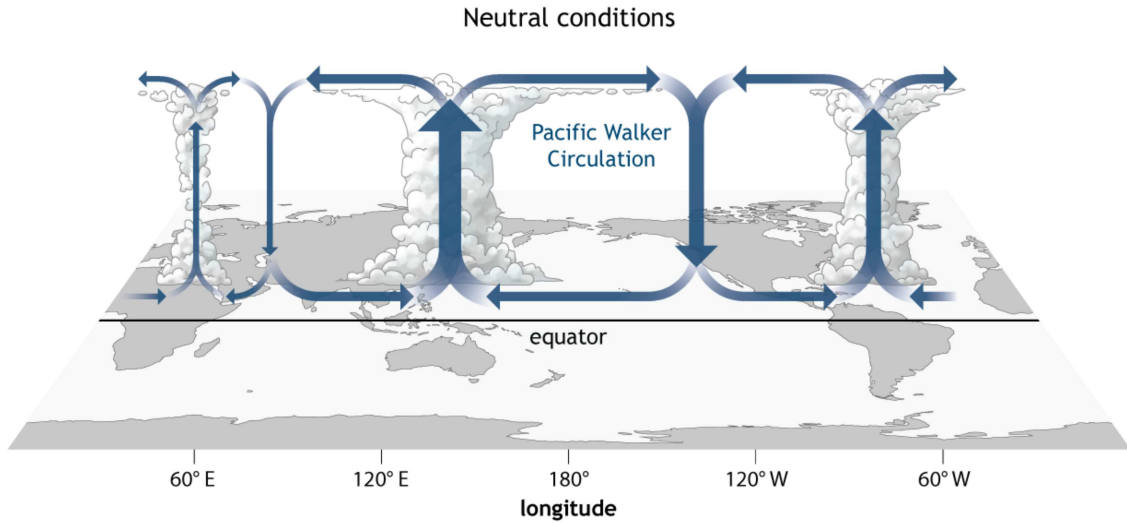
INTRODUCTION AND BACKGROUND

What happens in the tropics does not stay in the tropics. In fact, tropical processes are of great importance to weather and climate at higher latitudes. For example, latent heat released in the Intertropical Convergence Zone (ITCZ), the narrow band of deep convection that occurs as a result of convergence of the north and south trade winds near the equator, has a strong influence on the global circulation.

Perturbations to the tropical climate are important not only for the tropics, but also for global weather and climate. In particular, altering the tropical climate through Amazon deforestation may impact tropical latent heat release which impacts the ITCZ and therefore the global circulation. This study will focus on how deforestation of the Amazon rainforest can affect tropical sea surface temperatures (SSTs), especially in the eastern Pacific, by first influencing local rainfall and temperatures, which can then induce changes in large-scale circulations, including the Walker circulation.

Anomalously warm eastern Pacific SSTs are a characteristic of an El Niño event, which impacts atmospheric circulations and weather in the tropics and globally. During an El Niño event, rainfall over the Amazon is reduced and deep convection shifts from the west Pacific to the central and eastern Pacific. El Niño and its converse, La Niña, will be discussed in more detail later in this chapter. The perturbations to the location and intensity of deep convection associated with El Niño and La Niña affect latent heat release and as a byproduct, the global circulation.

A specific question that we will address is: Can Amazon deforestation enhance El Niño-like conditions? Studies often consider the impact of El Niño on tropical South American



NOAA Climate.gov

FIGURE 1.1. Schematic of the Walker circulation during neutral conditions. The main circulation loop occurs over the Pacific ocean and is defined by easterly trade winds, deep convection in the west Pacific, and broad subsidence in the east and central Pacific. Adapted from NOAA Climate.gov drawing by Fiona Martin.

climate and vegetation, but we are interested in the extent to which this coupling can work in reverse. We suspect that large-scale Brazilian deforestation can lead to warming of eastern Pacific SSTs by weakening the Walker circulation.

This chapter gives a brief introduction on tropical circulations and climate which are important for the climatic impacts of Amazon deforestation. Much of the discussion here can be found in Philander (1990).

1.1. THE WALKER CIRCULATION

The longitudinal (east-west) atmospheric circulation over the tropical Pacific is called the Walker circulation (Figure 1.1). Jacob Bjerknes was the first to use the term “Walker circulation” in 1969, naming it after Sir Gilbert Walker, who was known for his work on

the Southern Oscillation, or El Niño-Southern Oscillation (ENSO). The Southern Oscillation refers to the irregular oscillation in surface pressures between the tropical west and southeast Pacific (Lau and Yang 2015). These pressure fluctuations are associated with the two configurations of the Walker circulation mentioned previously, El Niño and La Niña. Walker also noted that these pressure fluctuations are related to patterns in rainfall and winds within the tropics and extend to regions outside of the tropics (Philander 1990). The Hadley circulation, the meridional counterpart of the Walker circulation, carries energy from the tropics to higher latitudes and is an important mechanism through which ENSO acts on regions outside of the tropics.

The Walker circulation, depicted in Figure 1.1, is characterized by an east-west Pacific sea surface temperature gradient, easterly (westward) surface trade winds, deep convection over the west Pacific ($\sim 130^\circ - 180^\circ$ E), a west-to-east return flow in the upper troposphere, and large-scale subsidence (sinking motion) over the central and eastern Pacific ($\sim 180^\circ - 130^\circ$ W). The Walker circulation can intensify through a positive feedback loop called the Bjerknes feedback, in which easterly trade winds reinforce the east-to-west sea surface temperature gradient which in turn strengthens the surface trade winds (stronger trade winds \rightarrow stronger SST gradient \rightarrow stronger trade winds). The trade winds support the SST gradient by pushing surface water from the east to west Pacific. The sun warms the surface waters as they travel westward, leading to an abundance of warm water near the maritime continent (Indonesia, Philippines, and Papua New Guinea). Cold, deep ocean water is brought to the surface (upwelling) in the eastern Pacific near the west coast of South America. The thermocline (the boundary between warm surface water and cold deep ocean water) deepens in the western Pacific due to the accumulation of warm water and shoals (shallows) in the

east. A shallower thermocline in the eastern Pacific is due to further upwelling of cold water, which then enhances the east-west SST gradient, the pressure gradient, and hence the surface trade winds (Wang et al. 2012).

The Walker circulation also includes secondary circulation loops (Figure 1.1) that extend to regions over South America ($\sim 130^\circ - 80^\circ\text{W}$) and the Atlantic Ocean as well as over the maritime continent and the Indian Ocean ($\sim 80^\circ - 130^\circ\text{E}$). The circulation loop over South America makes the connection between convection over the Amazon to the larger Walker circulation. This is how changes in vertical velocity over South America are linked to vertical velocities and the overall climate over the tropical Pacific. Weaker convection over South America, and hence weaker rising motion over the area, could weaken the subsidence that occurs over the central and eastern Pacific, leading to weaker trade winds and less intense convection over the west Pacific. This is the opposite (although still positive) mode of the Bjerknes feedback, in which weaker trade winds result in a decreased SST gradient and warmer eastern Pacific surface temperatures, further diminishing the trade winds (weaker trade winds \rightarrow weaker SST gradient \rightarrow weaker trade winds). There are thus two self-sustaining (via the Bjerknes feedback) configurations of the zonal circulation over the Pacific, a warm and a cold phase (El Niño and La Niña).

1.2. INTERANNUAL VARIABILITY IN THE TROPICAL PACIFIC

Year-to-year fluctuations in the weather of the tropical Pacific are mainly driven by the Southern Oscillation. The Walker circulation is usually in one of two states, either the cold phase of the Southern Oscillation, which is similar to the neutral Walker circulation depicted in Figure 1.1 (La Niña), or the warm phase of the Southern Oscillation (El Niño), which is

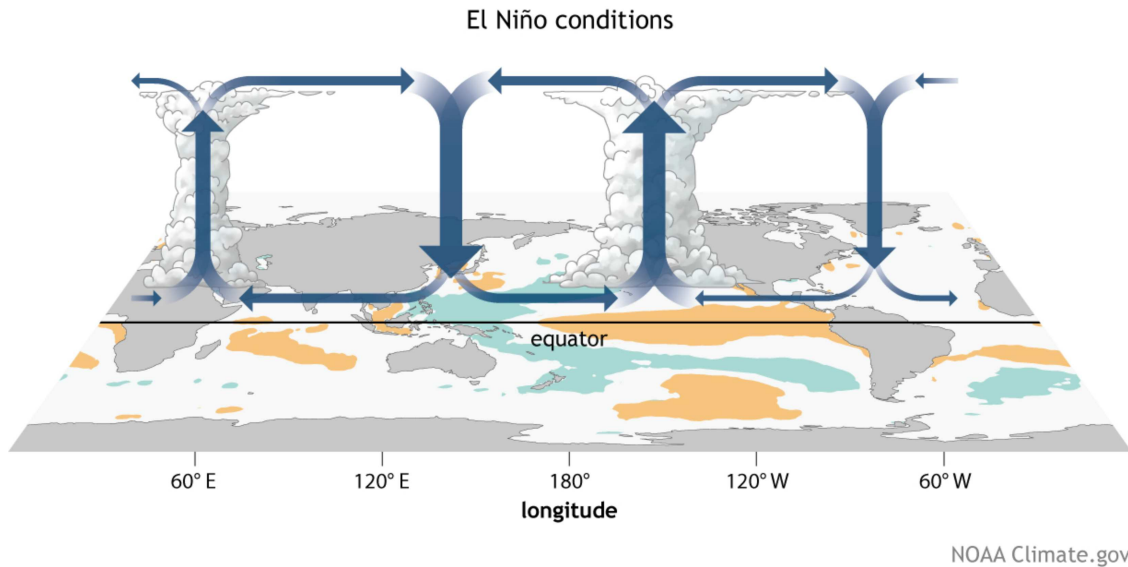


FIGURE 1.2. Schematic of the Walker circulation during the El Niño phase, where eastern Pacific SSTs are anomalously warm, trades are weak, convection is shifted from the west to central Pacific, and subsidence occurs over tropical South America. Adapted from NOAA Climate.gov drawing by Fiona Martin.

illustrated in Figure 1.2. During a La Niña the Walker circulation is intensified, characterized by stronger trade winds, an enhanced SST gradient across the equatorial Pacific, and intensified deep convection over South America accompanied by greater subsidence over the equatorial central and eastern Pacific. During an El Niño, the SST gradient, surface trade winds, and Amazonian precipitation are all weakened. The deep convection that occurs over the west Pacific during La Niña or neutral conditions is shifted over the anomalously warm central and eastern Pacific which induces anomalous subsidence over South America (Figure 1.2), inhibiting deep convection and suppressing rainfall there. These phases are also associated with a seesaw in sea level pressure between the southeastern and western tropical Pacific, which is consistent with the easterly trade winds, west-Pacific deep convection, and central and east-Pacific subsidence components of the Walker circulation. The oscillations between El Niño and La Niña are irregular but have an average return time of about four

years. The return time can range from two to ten years (Philander 1990). The duration and intensity can also vary drastically between distinct El Niño or La Niña events.

As discussed in the previous section, the two phases of ENSO are self-sustaining via the Bjerknes feedback. A perturbation is needed to shift from a warm to a cold phase or vice versa. Initially, Bjerknes was unable to explain how one phase can switch to the other given this positive feedback (Philander 1990; Wang et al. 2012). El Niño is initiated by a weakening of the trade winds or a warming of the eastern Pacific. Some theories suggest that ENSO is a natural oscillation between unstable phases of the coupled atmosphere-ocean system. Others propose that an El Niño is initiated by noise from other events such as westerly wind bursts associated with the Madden-Julien Oscillation (Wang et al. 2012). Whether the fluctuations between El Niño and La Niña events are a product of natural oscillation, external forces, or a combination of both, the variability in Pacific SSTs are known to have an influence on global circulations and climate.

A study by Alexander et al. (2002) investigated the impact of ENSO on the global oceans via the “atmospheric bridge”, which works through the Walker and Hadley cells. Figure 1.3 shows the correlation between SST averaged over November, December, and January (NDJ) in the central equatorial Pacific ENSO region and global SST averaged over the following three months, February, March, and April (FMA). They chose NDJ for the ENSO SST because this is when El Niño peaks, and FMA for the global teleconnections because it takes a few months for the effects of ENSO to develop globally. The SST data came from surface and satellite observations. The correlation (or teleconnection) map shows a strong positive correlation extending over the central and eastern Pacific. Warm SST over the east and central Pacific are expected during an El Niño. The correlation map also demonstrates that

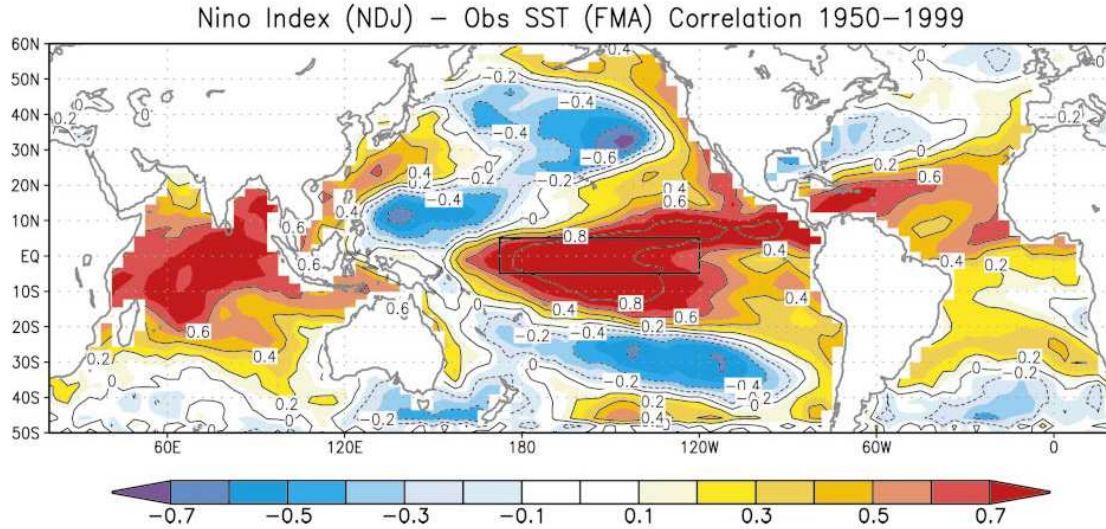


FIGURE 1.3. Correlation between SST anomalies in ENSO region for months NDJ and global SST for the following three months, FMA. Map from (Alexander et al. 2002).

significant connections between central Pacific SST and SST over remote regions, such as over the Atlantic and Indian Ocean, also exist. In addition to eastern Pacific SST having an impact on global SSTs, it also has a major influence over South American rainfall.

1.3. SST IMPACTS ON TROPICAL SOUTH AMERICAN PRECIPITATION

Many studies have connected El Niño to precipitation rates over tropical South America as well as regions throughout the globe (e.g., Ropelewski and Halpert 1987; Philander 1990; Fu et al. 2001; Marengo 2004). Areas that usually see dry desert conditions, such as the Peruvian coast of South America (west of the Andes), are transformed into lush environments during an El Niño, while the Amazon rainforest endures drought conditions. During El Niño years, the eastern Pacific is anomalously warm, which displaces convection and rising motion to the central and eastern Pacific. This induces subsidence over the Amazon by altering the Walker circulation. The increased subsidence over Brazil during El Niño years suppresses

convection and decreases precipitation rates. Although Pacific SSTs are responsible for a significant portion of the variability in rainfall over tropical South America, they cannot account for all of it. SST anomalies over the Atlantic ocean have also been linked to tropical South American precipitation (Nobre and Shukla 1996; Fu et al. 2001; Yoon and Zeng 2009; McGregor et al. 2014).

Pacific and Atlantic SSTs affect precipitation in different regions of the Amazon to varying degrees. Separating the relative impacts of the Pacific and Atlantic on Amazonian precipitation is difficult because Pacific SST anomalies associated with the El Niño-Southern Oscillation (ENSO) are correlated with both Amazon rainfall and Atlantic SSTs, so any correlation between Atlantic SSTs and Amazon precipitation could actually be an indirect influence of ENSO. Not only can ENSO influence Atlantic SSTs but Atlantic SSTs may also influence Pacific SSTs. A recent study by McGregor et al. (2014) looked at the impact of Atlantic SSTs on the Walker circulation and proposed that warming in the Atlantic in the early 1990s led to an intensification of the Pacific trade winds and Walker circulation resulting in cooler eastern Pacific SSTs. Both oceans are important for modulating rainfall variability over the Amazon.

Some studies have attempted to parse out the relative importance between Pacific and Atlantic SSTs on Amazonian precipitation (Fu et al. 2001; Yoon and Zeng 2009). Fu et al. (2001) concluded that the seasonal variations of Atlantic SSTs have a larger influence over Brazilian rainfall rates than the seasonality of Pacific SSTs. They also found that the Atlantic influence is greatest over the eastern Amazon during the equinox seasons. Other studies look at the influence of anomalous Atlantic SSTs, rather than seasonality, on tropical South American rainfall (Nobre and Shukla 1996; Yoon and Zeng 2009). Yoon et al.

(2009) found that SST anomalies in the Pacific and northern Atlantic are comparable in their influence over tropical South American rainfall. Eastern Pacific SST anomalies alter Amazon precipitation via the Walker circulation as previously discussed, and SST anomalies in the Atlantic influence rainfall distribution in the Amazon through the latitudinal shifting of the Atlantic Intertropical Convergence Zone (ITCZ) towards anomalously warm waters. Warming of the north Atlantic shifts the ITCZ north, which induces subsidence over the Amazon and decreases moisture flux convergence over the region, resulting in a decrease in precipitation.

Changes in atmospheric circulations, along with changes in sea surface temperatures over the Pacific and Atlantic, are correlated to changes in precipitation over tropical South America. Studies of ENSO connections to the global circulation and climate often look at the correlation between SST over the central Pacific (Niño 3.4 region) and other global parameters. In the previous section, a teleconnection map between central Pacific (Niño 3.4) SST and global SST from Alexander et al. (2002) was presented (Figure 1.3). This same type of map can be made to illustrate the impacts of ENSO on global precipitation. The correlation map between Niño 3.4 SST (Niño 3.4 index) and global precipitation from Langenbrunner and Neelin (2013) is depicted in Figure 1.4. The map shows that warm SSTs in the Niño 3.4 region are associated with decreased precipitation over the Amazon rainforest and increased precipitation across the central and eastern equatorial Pacific (El Niño conditions).

Previous studies have mostly focused on this correlation in one direction: the influence of SST variability on Amazonian rainfall. In this study we would like to investigate the reverse of this correlation: the influence of tropical South American precipitation changes on

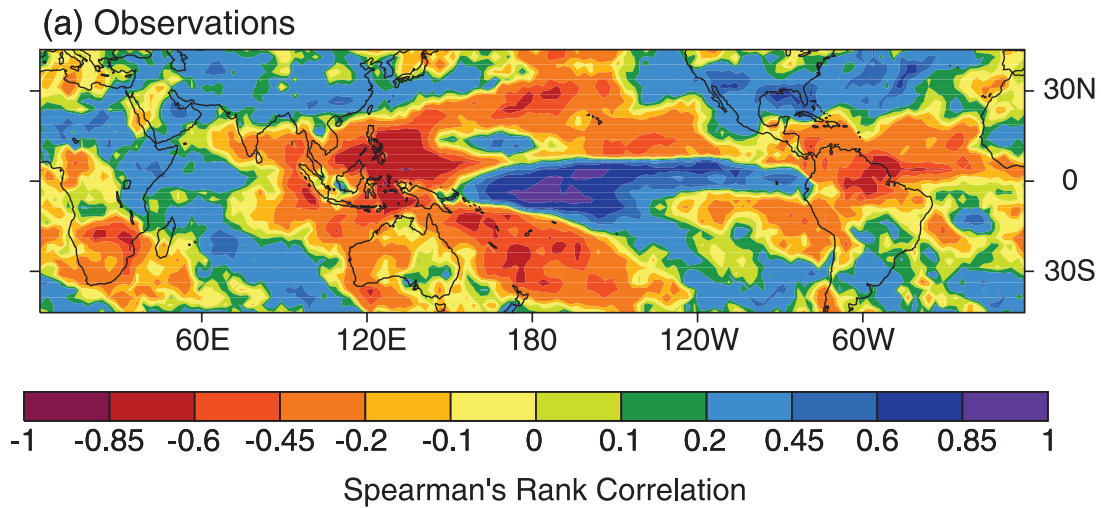


FIGURE 1.4. Spearman's rank correlation between the Niño 3.4 index and global precipitation. Adapted from (Langenbrunner and Neelin 2013).

surrounding ocean basins. Amazon drought and deforestation may affect local precipitation rates which could alter circulations over the Pacific and Atlantic and induce SST changes, which could then possibly amplify precipitation anomalies over the Amazon.

1.4. AMAZON DROUGHT, DEFORESTATION, AND CLIMATE CHANGE

Amazon deforestation is believed to have significant impacts on rainfall and temperatures over the region. Drought and deforestation in the Amazon rainforest have and will continue to have major consequences on local and global scales. Deforestation impacts the economy, local and global weather patterns, and species diversity. Amazonia is vast and is home to a substantial fraction of the world's animal and tree species (Mori and Prance 1987; Malhi et al. 2008). The trees in the Amazon also have a large impact on the carbon cycle. They provide a large sink for carbon of approximately $0.4 - 0.6 \text{ Pg C year}^{-1}$ and they account for about 25% of the carbon stored in the terrestrial biosphere (Bonan 2008; Malhi et al.

2008). During years of intense drought, such as in 2005 and 2010, the Amazon changes from a net sink of carbon to a net source (Phillips et al. 2009; Lewis et al. 2011; Bagley et al. 2014). Although the role of the Amazon forest in the global carbon cycle is of great importance, here we concentrate on the impacts of deforestation on circulation patterns and the consequences these changes will have for the future climate.

As discussed in the previous two sections, the Amazon is susceptible to intense drought in response to El Niño events as well as warm SST anomalies over the Atlantic. The Amazon rainforest has a high tolerance to these drought events. Trees in the Amazon can access soil water stored up to 10 m deep with their extensive roots (Nepstad et al. 1994; Nepstad et al. 2004; Malhi et al. 2008; Swann et al. 2015). Access to this water makes it possible for the rainforest to survive seasonal drought and provides moisture to the region during these times. Drought is a major threat to the Amazon forest and has possibly been enhanced in recent years by the ongoing deforestation. Several modeling studies of Amazon deforestation have found a lengthening of the dry season (Dickinson and Henderson-Sellers 1988; Nobre et al. 1991; Li et al. 2006; Malhi et al. 2008). More intense and frequent droughts in the Amazon weaken its inherent resiliency to dry periods. The lengthening of the dry season and reduction in dry season rainfall are extremely important for determining the fate of the Amazon. Precipitation rates heavily depend on water recycling and tree root access to deep water during the dry season in the Amazon. Moisture recycled from evaporation and plant transpiration in the Amazon rainforest contributes to a large fraction of the precipitation that falls there. Drought and deforestation also increase fire risks by drying and adding ignition sources, which is yet another threat to the forests of the Amazon.

An immediate consequence of deforestation through any means, whether natural or anthropogenic, is the change in albedo (fraction of shortwave solar radiation reflected from Earth's surface). Forests have darker surfaces and a lower albedo, while grasslands are brighter and have a higher albedo. The darker forests absorb more solar radiation, a warming effect, whereas a grassland reflects more solar radiation, a cooling effect. This cooling effect caused by an increase in albedo is counterintuitive to the surface warming that is expected to accompany deforestation. Although it is true that a brighter surface reflects more radiation, there are many more processes involved in the real world that accompany such a change in albedo. The impacts of surface albedo increase on rainfall in semi-arid regions (a transition from grassland to desert) were discussed by Charney et al. (1977). The increase in albedo initially decreases the amount of absorbed solar radiation at the surface by reflecting more sunlight, but this has the effect of decreasing surface sensible and latent heat fluxes. The consequent decrease in latent heat flux leads to an overall decrease in upward vertical motion and low-level horizontal convergence (or an increase in sinking motion and low-level divergence). The decrease in rising motion results in decreased convective cloud amount, which allows more sunlight to reach the ground, working against the initial cooling. The increase in incoming solar radiation is partially counteracted by a decrease in downwelling longwave radiation due to the reduction in clouds and water vapor, which exceeds the magnitude of increase in solar insolation. The overall effect of the albedo increase, according to Charney et al. (1977), is a decrease in net surface radiative flux (decreased absorption of solar plus longwave radiation by the surface). A decrease in net surface radiation absorption does not necessarily mean a decrease in surface temperature. Another finding of their study was that surface temperature increased from the cases with high evapotranspiration and low

albedo (grassland) to the cases with low evapotranspiration and high albedo (desert). So, in the case of deforestation, where evapotranspiration (sum of evaporation and transpiration from plants) would decrease due to the decrease in vegetation, local surface temperatures are expected to increase. The concepts in the Charney study also apply to ours, but caution must be exercised in directly comparing the two studies because Charney et al. looked at the conversion of grassland to desert and we are interested in the conversion of forest to grassland.

Another immediate and direct impact of deforestation is a decrease in the surface roughness length. The most obvious implication of decreasing surface roughness length is its impact on surface wind speeds. Surface wind speeds are much stronger over grassland than a forest, where wind flow is obstructed by the presence of tall trees. A decrease in roughness increases the aerodynamic resistance of the atmosphere, which has implications for evaporation and transfer of turbulent fluxes away from the surface. Early studies of tropical deforestation stressed the importance of surface roughness changes associated with deforestation and its impacts on turbulence and momentum and energy transfer between the surface and the atmosphere (Dickinson and Henderson-Sellers 1988; Lean and Warrilow 1989). Decreasing surface roughness reduces turbulent motion and the energy transfer between the surface and the atmosphere. This decrease in turbulence results in warming of the surface due to decreased efficiency of latent and sensible heat flux transfer to the atmosphere. More recent studies that use higher resolution and improved parameterizations of land-atmosphere processes support the conclusion of earlier studies that decreased surface roughness as a result of deforestation contributes to surface warming (Nobre et al. 1991).

As stated earlier, evapotranspiration (evaporation plus transpiration) is expected to decrease over a deforested area. Transpiration, the evaporation of water transported from the soil through plants via stomata (plant pores), decreases partly as a result of the decrease in leaf area index (leaf area per unit ground surface area) between grassland and forest. The leaf area index of grassland is much smaller than that of a forest (narrow blades of grass vs. broad leaves). Transpiration also decreases because there is less water available to a grassland than to a forest. Trees have deep, extensive root systems that can access water stored deep beneath the ground surface, whereas grasses have shallower roots and limited access to deep ground water (Nepstad et al. 1994; Swann et al. 2015). The evaporation in evapotranspiration accounts for evaporation from the ground as well as evaporation of water stored on the canopy (vegetation). The decrease in evaporation from the canopy surface can also be explained by the decrease in leaf area index. Less water is stored on the canopy in a grassland because interception of precipitation is smaller in comparison to that in a forest. Evaporation of soil water in a grassland decreases because the top soil layers are drier than in a forest. The reduction in evapotranspiration as a result of deforestation leads to a local decrease in precipitation. The majority of the moisture available for precipitation over the Amazon rainforest comes from transpiration of vegetation in the region (Salati and Nobre 1991). It is possible that a decrease in evapotranspiration does not necessarily correspond to a decrease in precipitation because moisture could be brought in from the surrounding ocean basins, but given that most Amazon precipitation is attributed to local recycling of moisture and evapotranspiration processes, we expect a decrease in precipitation in response to Amazon deforestation. Several studies have also supported this hypothesis, finding that

Amazon deforestation not only leads to a decrease in evapotranspiration but also a decrease in moisture flux convergence (Charney et al. 1977; Nobre et al. 1991; Malhi et al. 2008).

Latent and sensible heat fluxes are also subject to change in response to deforestation. Net surface radiative flux decreases, as discussed previously, due to the larger albedo over grassland. The net surface energy balance is the sum of radiative (shortwave and longwave) and turbulent (latent and sensible heat) fluxes. Surface latent heat decreases as a result of decreased leaf area index, rooting depth, and evapotranspiration. Latent and sensible heat transfer from the surface to the atmosphere decreases as a result of increased aerodynamic resistance of the atmosphere in response to the decreased surface roughness caused by deforestation. A decrease in the latent heat flux would favor a decrease in convection and rainfall, and a decrease in the sensible heat flux, would in turn lead to warming of the surface.

Decreased rainfall and evapotranspiration accompanied by increased surface temperature have been found by many modeling studies of Amazon deforestation (Dickinson and Henderson-Sellers 1988; Nobre et al. 1991; Nobre et al. 2009; Bagley et al. 2014). Although many studies agree that deforestation results in decreased precipitation, a review by D’Almeida et al. (2007) contrasts the precipitation response to Amazon deforestation in modeling studies carried out on different scales and resolutions. In particular, they found that macroscale modeling studies of complete Amazon deforestation found a general decrease in precipitation and evapotranspiration, whereas mesoscale modeling studies found that precipitation increased along the boundary of a forest and a deforested area.

D’Almeida et al. (2007) also commented on the importance of the spatial scale and pattern of deforestation on rainfall. The impacts of the spatial arrangement and magnitude of deforestation were tested in a previous modeling study of Amazon deforestation by Nobre

et al. (2009). They tested four different scenarios: a control run with no deforestation over the Amazon, a $1.85^\circ \times 1.85^\circ$ checkered pattern of 50% deforestation, a $5.5^\circ \times 5.5^\circ$ checkered pattern of 50% deforestation, and 100% deforestation over a large domain in the Amazon. These deforestation scenarios were run with an atmospheric general circulation model (AGCM) and a coupled general circulation model (CGCM; coupled atmosphere and ocean). Nobre et al. (2009) found systematic differences between the 50% deforestation simulations with different mesh grid sizes, indicating that continuity of deforestation is also an important factor in the atmospheric response to deforestation. Both models (AGCM and CGCM) simulated a local decrease in precipitation and warming of surface temperatures, but the coupled model gave even greater decreases in local precipitation and enhanced warming over the deforested region as well as warming that extended over the equatorial eastern Pacific. Another important finding of their study was the role of the ocean in enhancing the climatic response over land to deforestation. This is an aspect we will concentrate on in our study as well. Understanding the oceanic response to deforestation, especially to the west of the continent (in the eastern Pacific) is important to understand how Amazon deforestation can impact climate on a global scale. Adjustment of sea surface temperatures over the tropical Pacific are associated with El Niño and La Niña events.

It is no surprise that disturbing the massive Amazonian biome can have tremendous consequences. Although the effects of Amazon deforestation are many, this paper will focus on the role of the Amazon rainforest in driving global circulations and the impacts that forest loss can have on local and global climate. A main focus, which sets this study apart from previous Amazon deforestation studies, is that we are mainly concerned with the impact that Amazon deforestation can have on SSTs in surrounding basins. We hypothesize that

Amazon deforestation can have significant impacts on SSTs in the eastern Pacific as well as the Atlantic. Modifying SSTs in surrounding basins can have impacts on global circulation patterns (e.g. the Walker circulation) that can further impact weather and climate over tropical South America and also impact global climate patterns.

1.5. OUTLINE

In Chapter 2 we will discuss teleconnections (correlations) between Amazon precipitation and the Pacific climate, which emphasize the importance of atmosphere, ocean, and land couplings. In Chapter 3 we will discuss the model and methods used to carry out numerical simulations of hypothetical deforestation scenarios. Chapter 4 will provide discussion and results of the deforestation simulations. Chapter 5 will provide conclusions and a brief summary of our work.

CHAPTER 2

TELECONNECTIONS

The relationship between Amazon rainfall and global weather can be illustrated using teleconnection maps, which show the correlations between a parameter in a specific region and the same or a different parameter in other regions. These types of maps are often used in atmospheric science to describe how the weather in one location is related to the weather in a geographically different location. In the teleconnection maps shown here, the base point is average annual rainfall rates averaged over a domain in the Amazon basin, and the parameters that this is correlated to are: global temperature, precipitation, low cloud amount, 500 hPa vertical velocity, surface zonal winds, and 200 hPa zonal winds. In order to calculate these correlations, we use observational and model data from several different sources.

2.1. OBSERVATIONS

2.1.1. DATA.

2.1.1.1. *GPCP and GPCC Precipitation Data.* The dataset used for calculating the annual average of Amazon precipitation for years 1979 to 2009 was the Global Precipitation Climatology Centre (GPCC) full data product version 7 monthly precipitation data with a spatial resolution of $1^\circ \times 1^\circ$. This data is a combination of two distinct rain gauge datasets. The first makes up the years 1901 to 2010 and comes from land-based precipitation data from 67,200 stations around the world that have records of 10 years or more. The second dataset consists of quality-controlled rain gauge measurements from $\sim 7,000$ stations for the years 2007 to present (Schneider et al. 2011). We used the GPCC precipitation data for

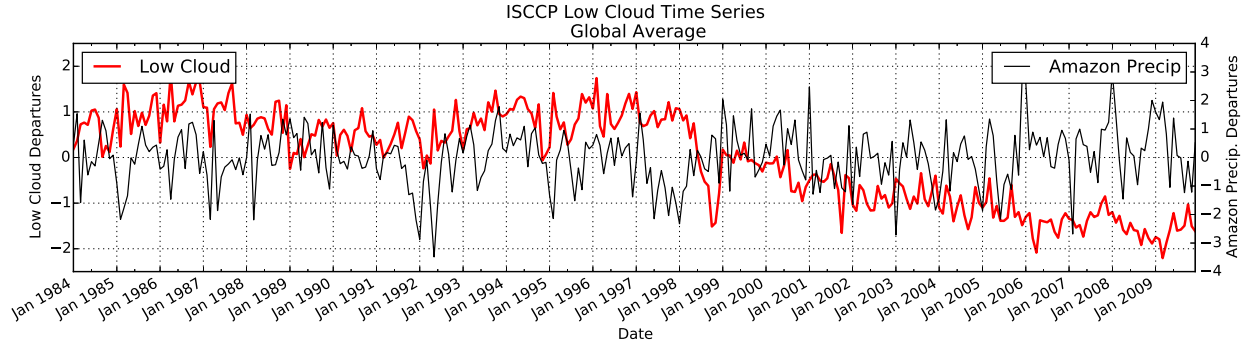


FIGURE 2.1. Time series of low cloud amount departures (from the climatological mean) from 1984 to 2009 (in red). Data comes from the International Satellite Cloud Climatology Project (ISCCP) dataset. Some studies suggest that the prominent decrease in low cloud amount starting in 1998 is not due to physical changes in the climate but rather a manifestation of satellite viewing geometry.

averages over the Amazon rainforest because it uses more land-based measurements than other datasets (e.g., GPCP, discussed in next paragraph) and has finer resolution over land. GPCP Precipitation data provided by the NOAA/OAR/ESRL PSD, Boulder, Colorado, USA, from their Web site at <http://www.esrl.noaa.gov/psd/>.

The World Climate Research Program (WCRP) created the Global Precipitation Climatology Project (GPCP) in order to provide a comprehensive global precipitation dataset that spans many years and utilizes various precipitation datasets. The second precipitation dataset used in this work is GPCP version 2.2 combined precipitation dataset, which is derived from several different satellite and rain gauge ($\sim 7,000$ stations worldwide) measurements (Adler et al. 2003). Data is retrieved for the years 1979 to 2009 and is on a $2.5^\circ \times 2.5^\circ$ global grid (Adler et al. 2003). GPCP precipitation data includes rainfall values over oceans, unlike GPCC, which was necessary to calculate global teleconnections to Amazon precipitation. GPCP Precipitation data provided by the NOAA/OAR/ESRL PSD, Boulder, Colorado, USA, from their Web site at <http://www.esrl.noaa.gov/psd/>.

2.1.1.2. *ISCCP Low Clouds*. Low cloud amount was obtained from the International Satellite Cloud Climatology Project (ISCCP) dataset. Data were collected via multiple satellites operated by various nations. The data obtained were D2 monthly averages of daily D1 ISCCP data and are on a 280 km equal-area grid resolution available from July 1983 to December 2009 (Rossow et al. 1996). Low cloud amount is defined as the fraction of cloudiness between the vertical levels 1000 hPa (Earth’s surface) and 680 hPa. One potential issue with using this dataset for our analysis is a significant decrease in global cloud amount starting in the late 1990’s and continuing to the end of the observing period, as seen in Figure 2.1. Evan et al. (2007) suggest that this observed decrease in cloud amount within the ISCCP dataset is due to artifacts of satellite geometry rather than a physical change in Earth’s atmosphere. They parsed out different regions and isolated a specific area where a geostationary satellite was introduced around the time of prominent decrease in cloud amount in the late 1990s and compared to an area outside of the range of this satellite. The time series of the region covered by the new geostationary satellite showed a sharp decrease in cloud amount and the other region showed a steady time series of cloud amount. They argue that although polar orbiting satellites also suffer from satellite viewing geometry, they are averaged out over several days, but the bias from geostationary satellites accumulate over the viewing period which may result in an unphysical signal in the long term trend of cloud amount. For our analysis we used the years 1984 through 1997 to eliminate possible bias from satellite viewing geometry.

2.1.1.3. *ERA Interim Reanalysis*. The European Center for Medium-Range Weather Forecasting (ECMWF) provides global atmospheric reanalysis from 1979 to present day.

Reanalysis data uses both observational and model data to provide a consistent and comprehensive dataset. The ERA-Interim dataset includes higher resolution (T255 spectral resolution ($\sim 80\text{km}$) on 60 vertical levels) and improved representations of the hydrological cycle, the quality of the stratospheric circulation, and the consistency in time of the reanalyzed fields in comparison to the previous ERA-40 dataset, whose place it has taken (Dee et al. 2011). All other “observational” data, other than that previously described, came from this product.

2.1.2. RESULTS. The interdependence between Amazonian rainfall and the Walker circulation is clearly seen in the teleconnection maps (Figure 2.2). These maps illustrate the correlation between precipitation averaged over the Amazon and atmospheric parameters related to the Walker circulation (surface temperature, precipitation, low cloud amount, mid-level vertical velocity, surface zonal wind, and upper tropospheric zonal wind). The correlation between Amazon precipitation and global SST shows a strong negative correlation over a broad triangular region in the eastern and central equatorial Pacific (Figure 2.2a), which means that a rainy Amazon is coeval with cold SSTs in that region. This map (Figure 2.2a) is almost the same as the map (but opposite sign) presented in chapter 1 (Figure 1.3). The difference here is that we are calculating the correlation between Amazon precipitation and global SST rather than Nino3.4 SST and global precipitation. We see a broad region of negative correlation over the central and eastern Pacific because Amazon rainfall is consistent with cooler eastern Pacific SSTs (La Niña conditions). The similarity between these two maps confirms the strong codependency between tropical Pacific SSTs and Amazon rainfall.

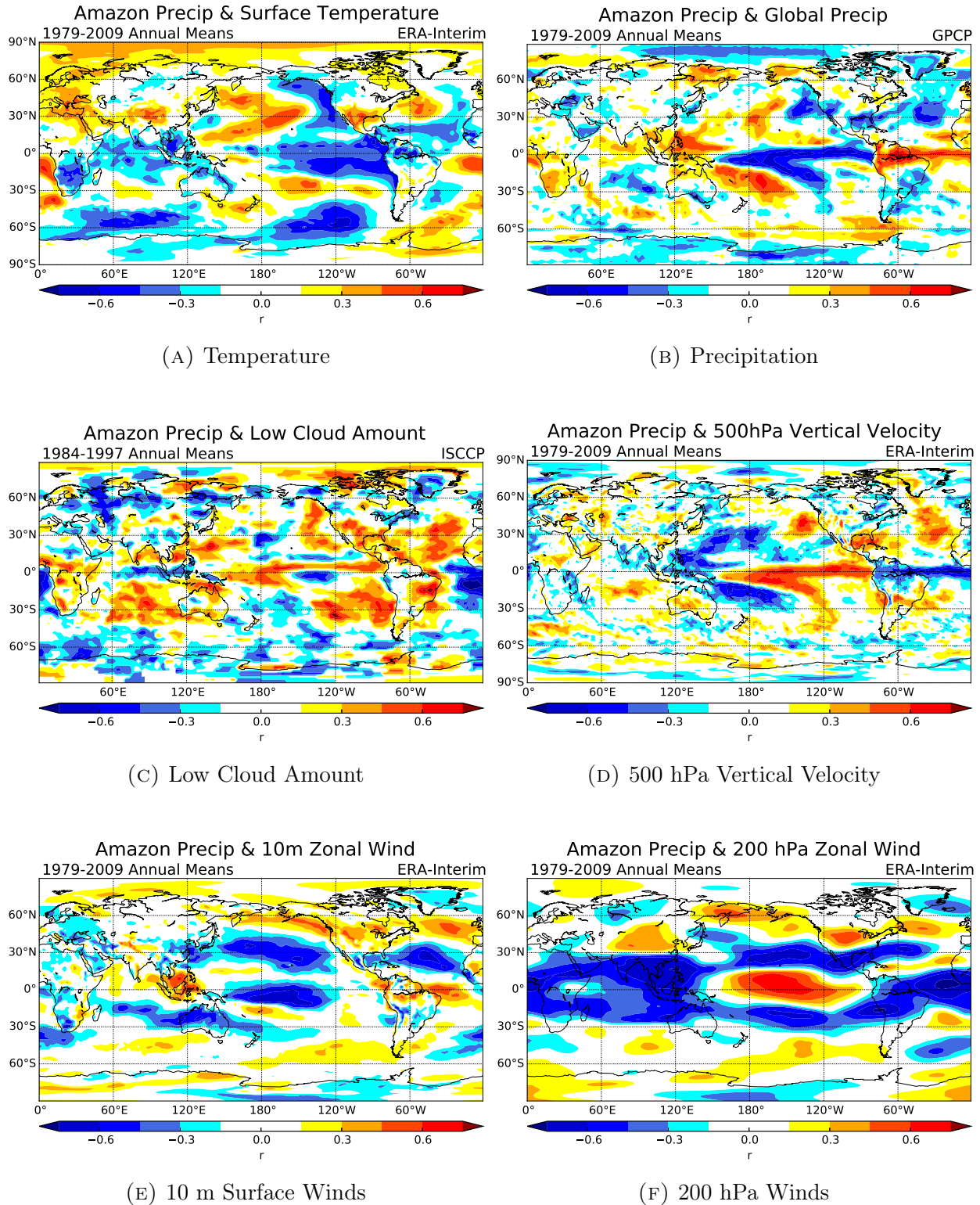


FIGURE 2.2. Teleconnection maps showing correlation between average annual Amazon precipitation and (a) temperature, (b) precipitation, (c) low cloud amount, (d) 500 hPa vertical velocity, (e) 10 m surface zonal wind, and (f) 200 hPa zonal wind for observational and reanalysis data.

The teleconnections between Amazon precipitation and global precipitation (Figure 2.2b) mirror the teleconnections with that of 500 hPa vertical pressure velocity (Figure 2.2d). Areas of negative correlation with precipitation show up as positive correlations with vertical velocity. A boomerang shape of negative correlation in precipitation is seen over the equatorial Pacific in Figure 2.2b. Amazon rainfall is concurrent with suppressed rainfall over the equatorial and central Pacific along with sinking motion at the 500 hPa level (Figure 2.2d). This map (Figure 2.2b) closely resembles Figure 1.4. The correlations are again opposite in sign (although the colorbars in both figures are reversed) because in contrast to the figure from chapter 1, which shows the correlation between the Niño 3.4 index (SST) and global precipitation, here we correlate Amazon precipitation to global precipitation. The teleconnection maps presented in chapter 1 (Figures 1.3 and 1.4) are depictions of El Niño conditions (warm SST), whereas our teleconnection maps (2.2) are portrayals of La Niña conditions (increased Amazon rainfall). The parallelism between ENSO teleconnection maps, which often use Niño 3.4 SST, and our teleconnection maps which use Amazon precipitation, further confirm that Amazon precipitation and eastern Pacific SSTs are closely interrelated.

Amazon rainfall also occurs when there are marine stratocumulus clouds in the eastern Pacific (over region of cold SST) as seen in the teleconnection map with low cloud amount (Figure 2.2c). The actual strength of the Walker circulation when the Amazon is wet can be investigated by looking at the surface and upper tropospheric zonal wind. The surface zonal wind is negatively correlated with Amazon precipitation over the central Pacific (Figure 2.2e). The negative correlation illustrates that surface zonal wind is easterly (westward) when the Amazon is rainy. The 200 hPa zonal wind shows a strong positive correlation

(Figure 2.2f) over the central equatorial Pacific, indicating that westerly upper tropospheric winds are stronger when the Amazon is wet.

The teleconnection maps in Figure 2.2 show that rain in the Amazon is concurrent with: lower surface temperatures, decreased precipitation accompanied by increased subsidence and marine stratocumulus clouds, and stronger Walker circulation characterized by strong westward surface zonal winds and eastward upper tropospheric zonal winds extending over the central equatorial Pacific. These relationships: strong trade winds, broad subsidence over the eastern Pacific, are all consistent with a strong Walker circulation in the La Niña phase, which is also consistent with high rainfall rates over Amazon.

2.2. AMIP & CMIP5 DATA

2.2.1. MODELS AND DATA. To get an idea of how climate models represent the Walker circulation and the coupling to Amazon precipitation, we made the same maps using model data from phase five of the the Coupled Model Intercomparison Project (CMIP5). CMIP was created to fill major gaps in the historical atmospheric record and to attempt to answer several questions that emerged from the Intergovernmental Panel on Climate Change (IPCC) Fourth Assessment Report (AR4) (Taylor et al. 2012). The CMIP5 framework consists of many models that include coupled ocean-atmosphere processes (an ocean model coupled to an atmospheric model). Although these models have the capability to run with a coupled ocean, we retrieved data that used the Atmospheric Model Intercomparison Project (AMIP) experimental protocol, which omits the coupled ocean and ice models. AMIP experiments are run using prescribed sea ice and sea surface temperatures (SSTs) according to observations from 1979 to present (Gates et al. 1999). Using prescribed SSTs rather than an ocean model

ensures that the correct seasonality and interannual variability (e.g. El Niño events) of the SST are included. We want to see how well the model can simulate the rainfall over the Amazon given observed SSTs.

The two models we chose were the Community Climate System Model version 4 (CCSM4) created in Boulder, Colorado (Gent et al. 2011) and the Model for Interdisciplinary Research on Climate version 5 (MIROC5) developed in Japan (Watanabe et al. 2010). The data from CCSM4 used an approximately 1-degree horizontal resolution ($0.9^\circ \times 1.25^\circ$) for the land and atmosphere with 26 atmospheric levels. MIROC5 was run using a horizontal resolution of T85 ($\sim 1.4^\circ$ at equator) for land and atmosphere with 40 vertical levels in the atmosphere.

2.2.2. RESULTS. The teleconnection maps illustrating the correlations between Amazon precipitation and the same variables as previously used for observations are shown in Figures 2.3 and 2.4 for CCSM4 and MIROC5 data, respectively. Both models capture the general structure of the teleconnection patterns over the tropical Pacific Ocean that are seen in observations (Figure 2.2). The strengths of the correlations are greater for the model data than for the observations, perhaps because the real world is much more complicated than the world as represented in atmospheric models. Volcanoes and forest fires are examples of real world complexities that are not represented in these models. Both the CCSM4 and MIROC5 models seem to capture the coupling between precipitation over the Amazon and the Walker circulation fairly well. The structure of the CCSM4 teleconnection maps appear to have a simpler structure than the MIROC5 teleconnections, which more closely resemble the observational teleconnections, especially for correlations with precipitation (Figure 2.4b) and 500 hPa vertical velocity (Figure 2.4d). One major difference between the CCSM4 and the MIROC5 teleconnection maps are the low cloud amounts (Figures 2.4c and 2.4c). Global

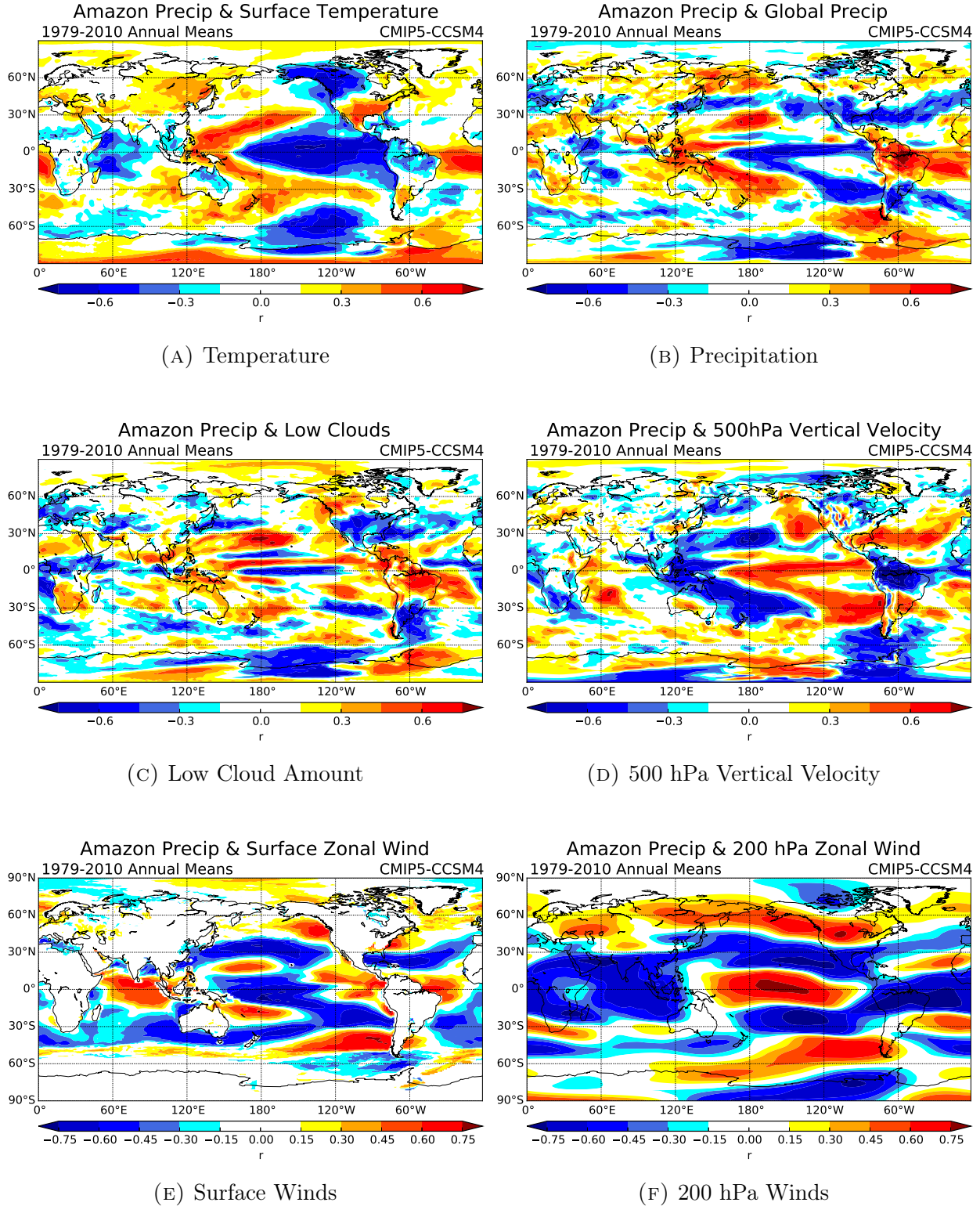


FIGURE 2.3. Teleconnection maps showing correlation between average annual Amazon precipitation and (a) temperature, (b) precipitation, (c) low cloud amount, (d) 500 hPa vertical velocity, (e) surface zonal wind, and (f) 200 hPa zonal wind for CCSM4.

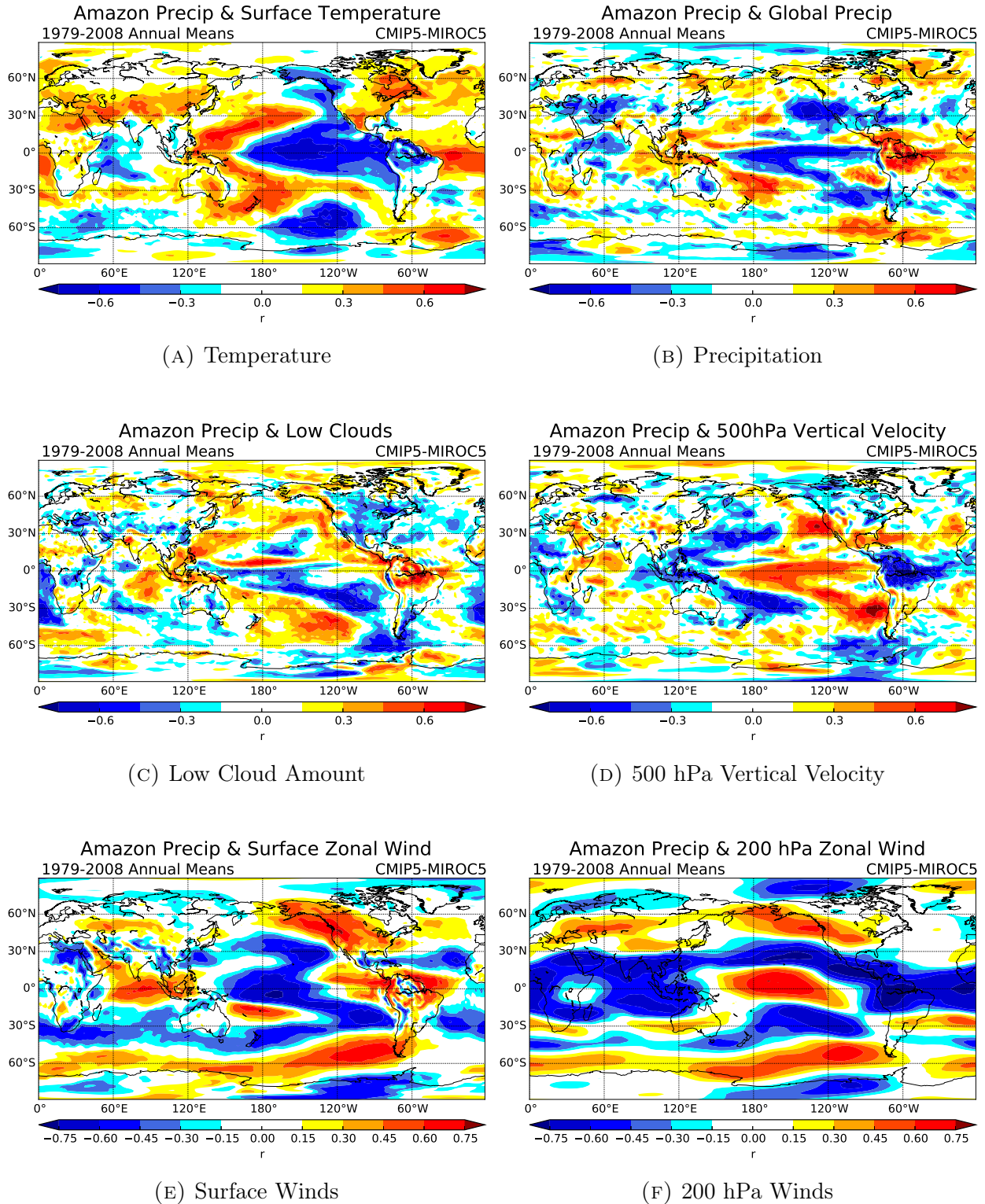


FIGURE 2.4. Teleconnection maps showing correlation between average annual Amazon precipitation and (a) temperature, (b) precipitation, (c) low cloud amount, (d) 500 hPa vertical velocity, (e) surface zonal wind, and (f) 200 hPa zonal wind for MIROC5.

circulation models (GCMs) are known to have difficulty representing clouds due to coarse vertical resolution of the model. Marine stratocumulus clouds are very thin in the vertical direction, and very widespread in the horizontal. The teleconnection map for MIROC5 low cloud amount (Figure 2.4c) shows a strong negative correlation in the eastern and southeastern Pacific, where we expect to see a positive correlation. The vertical resolutions between CCSM4 and MIROC5 are very different, which is likely the cause of the striking differences in the low cloud amount teleconnection maps. As discussed earlier, there are also problems with observational cloud data due to biases in satellite viewing angles, so caution must be exercised when analyzing data involving clouds and cloud amounts.

2.3. CESM AMIP SIMULATION

2.3.1. MODEL DESCRIPTION. We also did a similar analysis using the Community Earth System Model (CESM1.1.1), which is the model chosen to run numerical experiments in this study. Because this is the model we used for our simulations, we wanted to test its ability to simulate the Walker circulation and its coupling to precipitation over South America. The CESM was run using the AMIP experimental protocol with fixed SSTs and sea ice. CESM1.1.1 succeeds the CCSM4 discussed in the previous section. Improvements made from CCSM4 to CESM1.1.1 include a fully coupled carbon cycle and the ability to simulate changes in the Greenland Ice Sheet (Hurrell et al. 2013). The CESM includes models for the atmosphere, land, ocean, land-ice, sea-ice, and river-runoff. The different components can be combined and utilized in various ways. Most of the components have a data model functionality in which forcing data is provided by the user and read by the model. For our experiments, we used the data model for the ocean and sea-ice components, although an

active ocean model, the Parallel Ocean Program (POP), is provided. Fully active models are used for the atmosphere and land in our simulations. The atmosphere and land models within the CESM are the Community Atmosphere Model (CAM4) and the Community Land Model (CLM4.0). We used a coarser horizontal grid spacing of about 2-degrees ($1.9^\circ \times 2.5^\circ$) compared to the CCSM4 and MIROC5 data presented earlier. CAM4 uses bulk microphysics and has 26 levels. Version 4 of the CLM is used for all numerical experiments and has 10 soil levels.

2.3.2. RESULTS. The CESM is a successor of the CCSM4, so we expect CESM and CCSM4 to have similar capability in capturing the coupling between the Walker circulation and Amazon rainfall rates. Figure 2.5 illustrates the teleconnections between Amazon precipitation and the atmospheric parameters related to the Walker circulation. Overall, the correlations simulated by the CESM are pretty similar to observations. The same basic correlations to Amazon precipitation are seen with cold central and east equatorial SSTs, reduced precipitation over equatorial Pacific, presence of low clouds over the eastern Pacific, subsidence over equatorial Pacific and a stronger Walker circulation observed as strong surface and upper tropospheric zonal winds. A noticeable difference between the CESM correlations and the other teleconnection maps is that the lower flank of the “boomerang” shape that we see in the precipitation correlations is not as pronounced (Figure 2.5b). The band of precipitation that extends from the tropical west Pacific near Indonesia and Australia towards the southeastern Pacific is called the South Pacific Convergence Zone (SPCZ), which is related to the Intertropical Convergence Zone (ITCZ). The weaker correlation in the SPCZ region could mean that the CESM does not represent the SPCZ as well as the other models, at least with the coarse resolution used here.

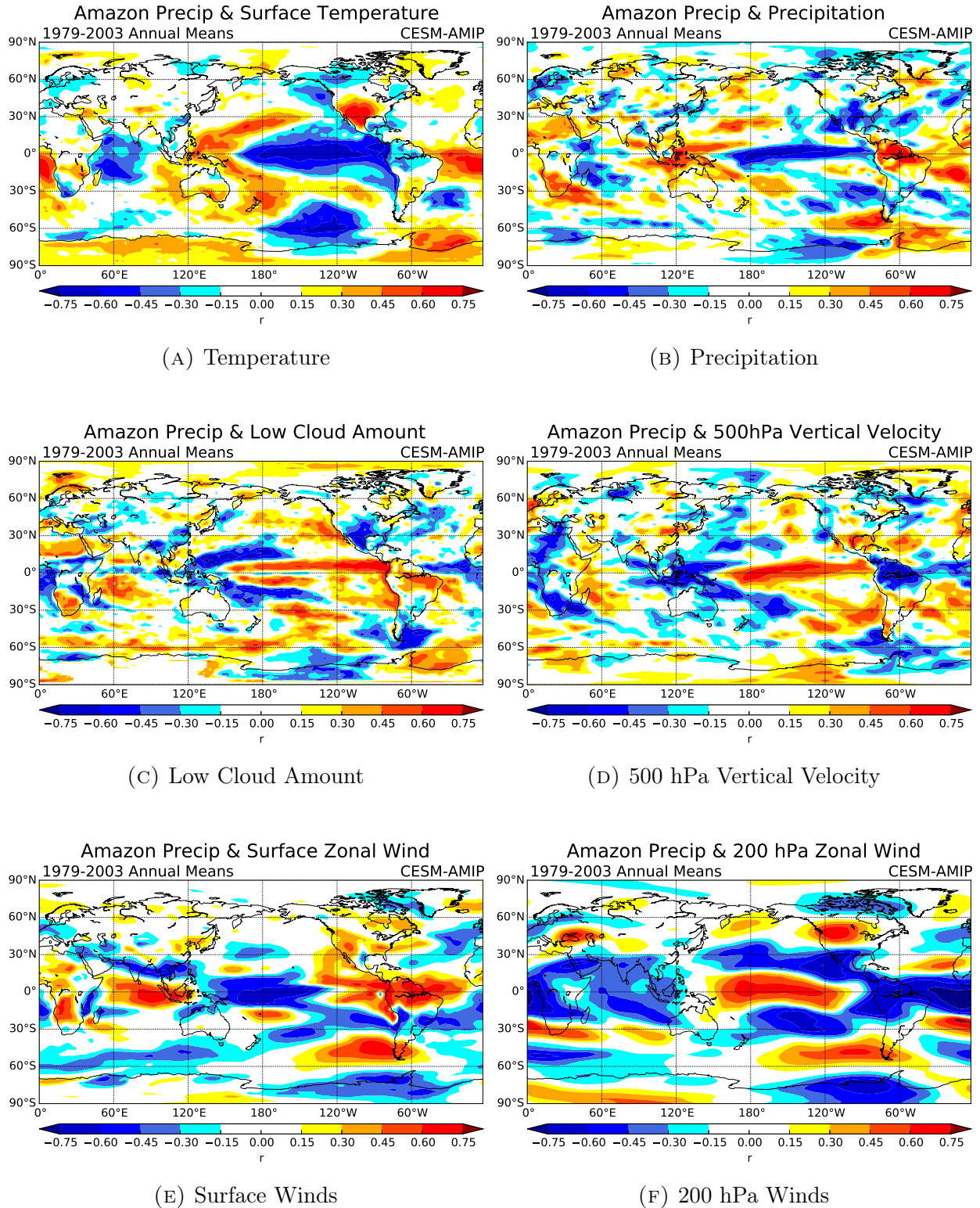


FIGURE 2.5. Teleconnection maps showing correlation between average annual Amazon precipitation and (a) temperature, (b) precipitation, (c) low cloud amount, (d) 500 hPa vertical velocity, (e) surface zonal wind, and (f) 200 hPa zonal wind for CESM1.1.1.

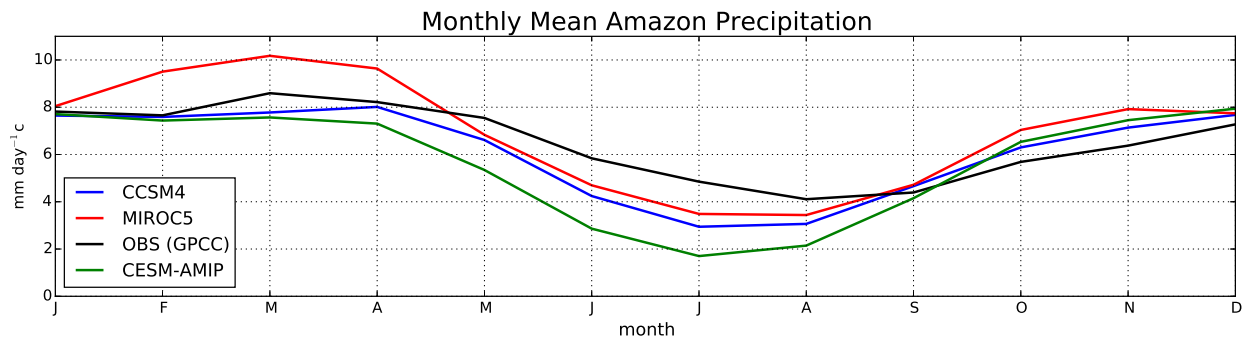


FIGURE 2.6. Monthly mean Amazon precipitation for observations from GPCC (black), CCSM4 (blue), MIROC5 (red), and CESM1.1.1 (green).

2.4. DISCUSSION

We have shown that models can successfully capture the coupling of Amazon rainfall to the Walker circulation, as seen in the teleconnection maps (Figures 2.2-2.5). Another question we can ask is: How well do the models simulate Amazon precipitation? The monthly mean Amazon precipitation for observations, CCSM4, MIROC5, and CESM1.1.1 are compared in Figure 2.6. All of the models are able to accurately capture the annual cycle of observational precipitation (black line). The CESM underestimates precipitation from about March-September slightly more than the CCSM4 and MIROC5 models. This underestimation is likely due to the coarser resolution used for CESM which is $\sim 1^\circ$ coarser than CCSM4 and MIROC5. We are not concerned with perfectly simulating the precipitation rates, we are mainly interested the precipitation trends and coupling to other processes. The teleconnection maps and closely simulated precipitation trends between the models and observations gives us confidence that the models are capable of simulating changes in the Walker circulation caused by deforestation-induced precipitation changes. These teleconnection maps also demonstrate the importance of ocean-atmosphere coupled processes in determining changes in rainfall rates and surface temperatures over the tropics.

CHAPTER 3

MODEL AND EXPERIMENTAL DESIGN

3.1. MODEL DESCRIPTION

The model used for numerical experiments in this study is the Community Earth System Model (CESM1.1.1), which was discussed in more detail in Chapter 2.3.1. The atmosphere and land models used in this study are the Community Atmosphere Model (CAM4) and Community Land Model (CLM4.0), which were also discussed earlier.

A superparameterized version of CAM (SP-CAM) is also used in this study. Superparameterization refers to the method of parameterization of moist convection and large-scale condensation in the model. In place of the conventional method of parameterization that is used in CAM, SP-CAM embeds a two dimensional cloud resolving model (CRM) within each grid cell of the CESM. Cloud fraction is explicitly calculated in the CRM, and is then used for radiation calculations. The CRM embedded within each grid cell of the CAM is the System for Atmospheric Modeling (SAM) Version 6.8.2 (Khairoutdinov and Randall 2001). SP-CAM can be run with either a single or double moment microphysics scheme. In the interest of keeping computational times low, we used the single-moment microphysics scheme in this study (consistent with CAM4). By default, the 2D CRM is oriented north-south within the grid cell. We expect precipitation and clouds to be simulated better using the SP-CAM.

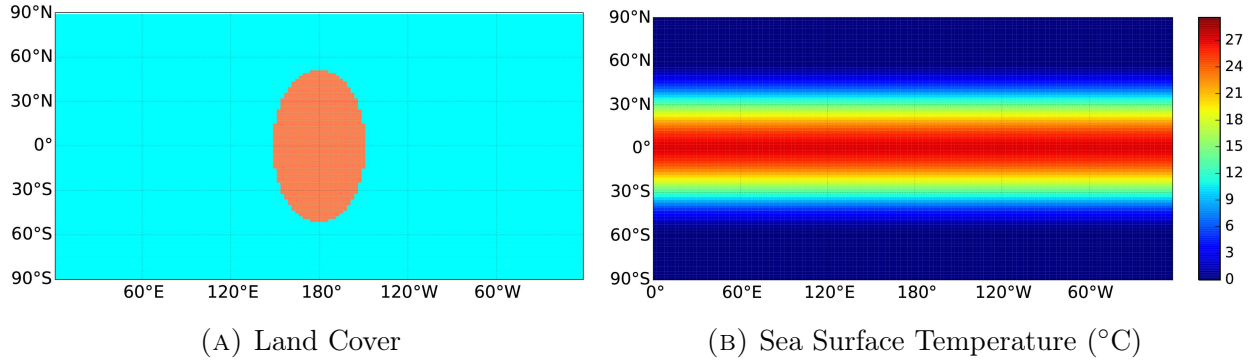


FIGURE 3.1. (a) Land cover and (b) sea surface temperature distribution for idealized simulations.

3.2. IDEALIZED SIMULATIONS

3.2.1. BASELINE SIMULATIONS. We carried out a series of idealized simulations in which we created an Earth-like planet with a single elliptical continent centered on the date line and bound by latitudes 50°N and 50°S and longitudes 150°E and 150°W (Figure 3.1a). The horizontal resolution was $1.9^{\circ} \times 2.5^{\circ}$ (~ 2 -degrees) for the land and atmosphere models. The surface elevation was set to 1 meter for the entire land mass. Two variations of this setup were run. The continent was covered in broadleaf evergreen tree (BET) forest for one simulation (FOREST) and covered in grassland in the other (GRASSLAND). The grid cell had 100% vegetation cover in the case for the forest and 65% cover in the grassland case (35% bare ground). C_4 grasses (adapted to hot seasonal conditions) were placed between 25°N and 25°S and C_3 grasses (adapted to cool seasons) were placed at latitudes greater than 25° . In addition to different plant functional types and vegetation cover, the two experiments also had different soil properties and surface characteristics which are defined in the input surface data file for the land model (CLM4.0). Among the surface characteristics that differ between the two runs are leaf area index (LAI), stem area index (SAI), soil texture (%sand, %clay, inferred %silt, and organic matter density), and soil color which determines saturated

TABLE 3.1. Difference in surface characteristics for FOREST and GRASSLAND simulations. (PFT=plant functional type; BET=broadleaf evergreen trees; C4=C₄ grass; C3=C₃ grass; LAI=leaf area index; SAI=stem area index; TOP=height top; BOT=height bottom)

Surface Characteristics	FOREST	GRASSLAND
soil color	16	11
soil texture (%) (clay/sand)	47/32	51/27
organic matter density (kg m ⁻³)	41.46	32.76
PFT	BET	C4; C3 latitudes >25°
vegetation cover (%)	100	65
max. fractional saturated area	0.43	0.37
LAI/SAI	4.62/0.82	0.73/0.48
TOP/BOT (m)	35/1	0.5/0.01

and dry soil albedos. The FOREST surface characteristics were based on values computed by averaging over a small domain in the Amazon rainforest where the fraction of broadleaf evergreen trees (BET) were close to 100%. For the GRASSLAND simulation we chose a small domain over the African savanna in order to define the surface characteristics. Values of different surface characteristics for the simulation pairs are given in Table 3.1.

The sea surface temperature (Figure 3.1b) was prescribed according to an aquaplanet distribution that is zonally symmetric (Neale and Hoskins 2000). The simulations ran with a perpetual equinox (perpetual day of the year) which was achieved by setting the obliquity and eccentricity of the planet to zero. We turned off the radiative effects of aerosols and prescribed the ozone profile to a zonally symmetric annual mean profile suitable for an aquaplanet simulation. Sea ice and the river transport model were also turned off. These simulations were run for 1,825 days with the first 365 days ignored to account for model

spin-up. A model simulation year is not supposed to mimic an Earth year because we have set a perpetual equinox and seasonal variability does not exist in our simulations.

3.2.2. SIMULATIONS WITH TOPOGRAPHY. The idealized set-up (with CAM4) was also run with idealized topography. The topography was constructed to represent an idealized version of the Andes. We used a two-dimensional Gaussian, Eq. (3.1), elongated in the north-south direction to create the topography file. In Eq. (3.1),

$$(3.1) \quad f(\lambda, \phi) = A \exp \left[- \left(\frac{(\lambda - \lambda_0)^2}{2\sigma_\lambda^2} + \frac{(\phi - \phi_0)^2}{2\sigma_\phi^2} \right) \right]$$

A is the peak amplitude, λ and ϕ are the longitude and latitude, λ_0 and ϕ_0 are the central longitude and latitude, and σ_λ and σ_ϕ are the longitudinal and latitudinal half-widths of the function. We used the following values for our idealized mountains: $A = 28,000 \text{ (m}^2\text{s}^{-2}\text{)}$, $\lambda_0 = 0^\circ$, $\phi_0 = 160^\circ$, $\sigma_\lambda = 3^\circ$, $\sigma_\phi = 10^\circ$. The mountain range is centered on the equator and 160°E , and extends from about 30°N to 30°S and 150°E to 170°E . An illustration of the idealized topography is given in Figure 3.2. Adding topography to our simulation allows us to investigate the relative importance and impacts of the Andes on the Walker circulation and precipitation over South America.

3.2.3. SIMULATIONS WITH A SLAB OCEAN MODEL. These idealized simulations were run again using a very simple slab ocean model (SOM). Using this set-up, we can get a better idea of how the ocean responds to changes in vegetation over land (e.g. Amazon deforestation). The equation used to calculate the SST of the ocean mixed layer is

$$(3.2) \quad \rho c_p h_{mix} \frac{dSST}{dt} = F_{net} - F_{net,FOREST}$$

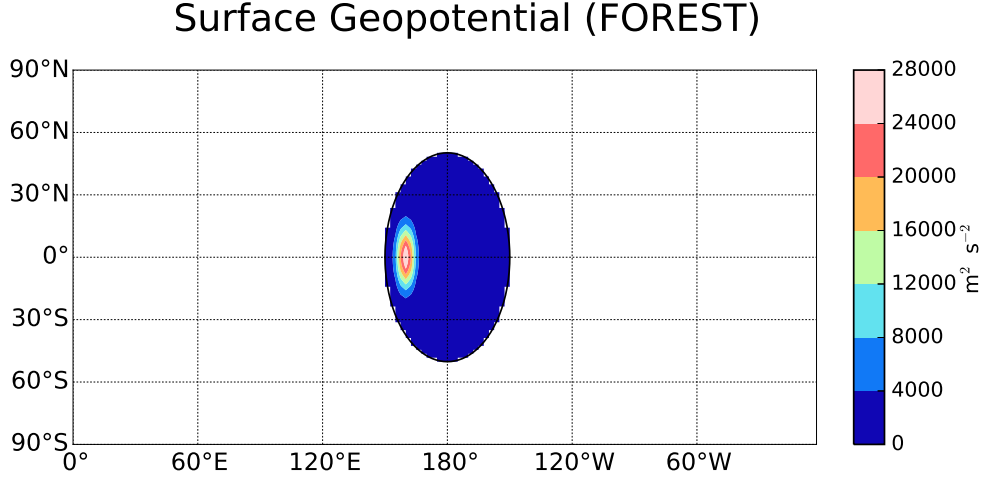


FIGURE 3.2. Surface geopotential of idealized topography in FOREST_TOPO and GRASSLAND_TOPO simulations.

Here, ρ is the density of water, c_p is the specific heat capacity of water, h_{mix} is the mixed layer depth, $dSST/dt$ is the change in sea surface temperature, F_{net} is the net surface heat flux, and $F_{net,FOREST}$ is the time-averaged net surface heat flux taken from the last 1,460 days of FOREST simulation. The mixed layer depth (h_{mix}) of the ocean was set to 5 meters everywhere.

A summary of our experiments is given in Table 3.2.

3.2.4. SIMULATIONS WITH SP-CAM. We continued the idealized simulations described in the previous section (FOREST and GRASSLAND) , but instead of using CAM4 for the atmospheric model, we used SP-CAM. These simulations (FOREST_SP and GRASSLAND_SP) were only run for 365 days, due to the increased computational expense of SP-CAM and decreased spin-up time. Because these experiments were continued from the previous idealized runs, we expect that a short spin-up will suffice, and ignore only the first 90 days of the simulation to account for model adjustment.

TABLE 3.2. Summary of numerical experiments performed in this study.

Experiment Name	Atmospheric Model	Simulation Length in Days	Description
FOREST	CAM4	1,825	single continent covered in forest
GRASSLAND	CAM4	1,825	single continent covered in grassland
FOREST_SP	SP-CAM	365	same as FOREST run with single moment SP-CAM
GRASSLAND_SP	SP-CAM	365	same as GRASSLAND run with single moment SP-CAM
FOREST_TOPO	CAM4	1,825	same as FOREST run with idealized topography
GRASSLAND_TOPO	CAM4	1,825	same as GRASSLAND run with idealized topography
FOREST_SOM	CAM4	1,825	same as FOREST run with 5m slab ocean
GRASSLAND_SOM	CAM4	1,825	same as GRASSLAND run with 5m slab ocean

CHAPTER 4

RESULTS OF IDEALIZED SIMULATIONS

4.1. BASELINE SIMULATIONS

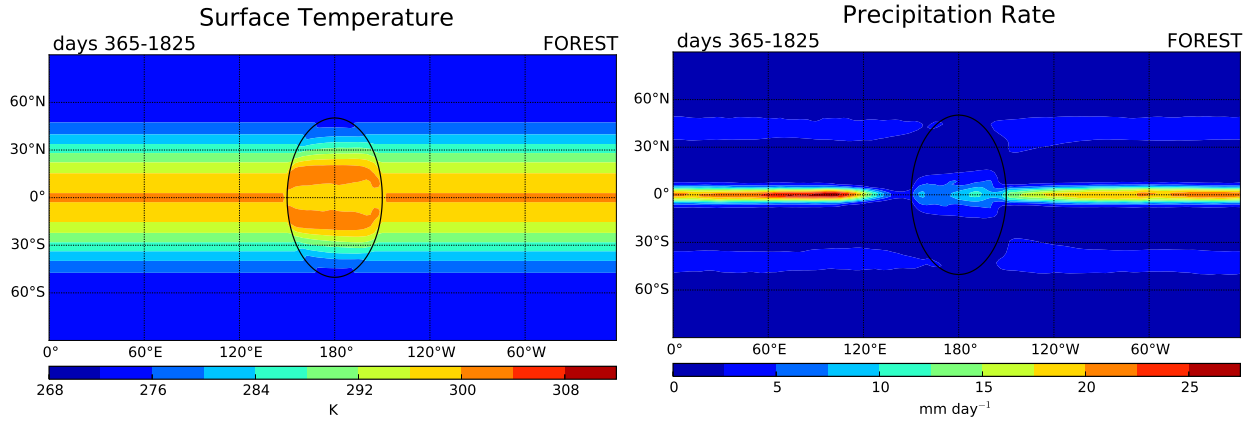
In our simulations we make connections between the Walker circulation seen in the real world to the circulation that occurs to the west of the continent in our simulations. Although they are not exactly the same, the circulation in our simulations has general similarities to the real Walker circulation. For example, in our simulations we see easterly surface winds and an upper tropospheric westerly return flow, which are similar to the winds seen to the west of South America in the Walker circulation.

We expect the atmosphere in the forest simulations to be comparable to La Niña-like conditions and the atmosphere in grassland simulations to exhibit El Niño-like behavior. The difference between these two simulations (GRASSLAND-FOREST) are analyzed as deforestation experiments. Recall that the teleconnection maps in Chapter 2 show La Niña conditions and our deforestation simulations are expected to show El Niño conditions. We can compare the teleconnection maps in Chapter 2 to our deforestation results (GRASSLAND-FOREST) to see if the responses appear opposite.

As mentioned previously, a change in the surface albedo is one of the most apparent and immediate impacts of deforestation. Soil albedo in the CLM is determined by the soil color variable in the input surface data file. Initially (and mistakenly), soil color was the same in both the FOREST and GRASSLAND simulations, which gave us only a 2% albedo difference between the two experiments, when based on previous modeling studies of deforestation, we expected an increase of about 6-9% (Dickinson and Henderson-Sellers 1988; Shukla et al. 1990). After fixing this issue and ensuring that the soil color was set

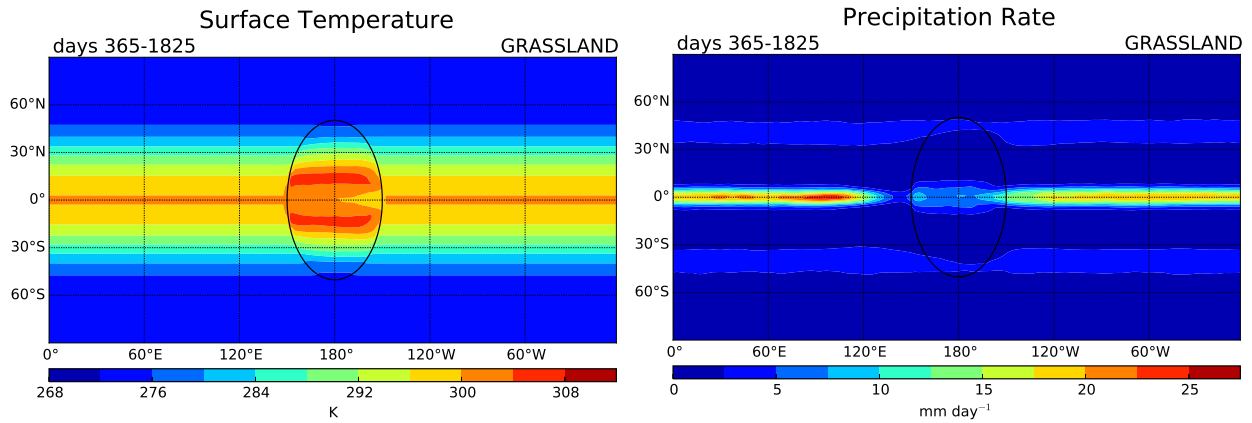
differently between the two simulations, we got an albedo difference of about 9%. Correcting the albedo and soil texture (%sand, %clay, %silt, and organic matter density) appeared to have slight but noticeable changes on the atmosphere. The most noticeable changes we saw after increasing the albedo difference between the two runs were on the precipitation. When the albedo was nearly the same between the FOREST and GRASSLAND simulations we observed an increase in precipitation over the continent along the equator surrounded by a region of decreased precipitation when looking at the difference between the two runs (GRASSLAND-FOREST). We also saw little change directly to the west of the continent near the equator and a decrease in precipitation a little further off the coast to the west of the land mass. After correcting the albedo, the area along the equator and over the land that previously showed an increase in precipitation disappeared and only a broad region of decreased precipitation from approximately 5°N to 25°S was observed. The response of precipitation to the west of the continent also showed an appreciable change. Where the simulations with 2% albedo increase presented very little change west of the continent and a decrease in precipitation a little further west from the coast, the simulations with 9% albedo increase showed a large region of noticeable increase in precipitation to the west of the continent going from forest to grassland. These differences demonstrate the importance that a significant surface albedo change can have on the atmosphere and climate, an impact also discussed in great detail in Charney et al. (1977). The precipitation to the west of the continent is of interest to us because precipitation anomalies in the eastern Pacific to the west of South America are linked to El Niño events.

Maps of the surface air temperature (K) and precipitation rate (mm day⁻¹) for the FOREST and GRASSLAND experiments are illustrated in Figure 4.1. The maps show



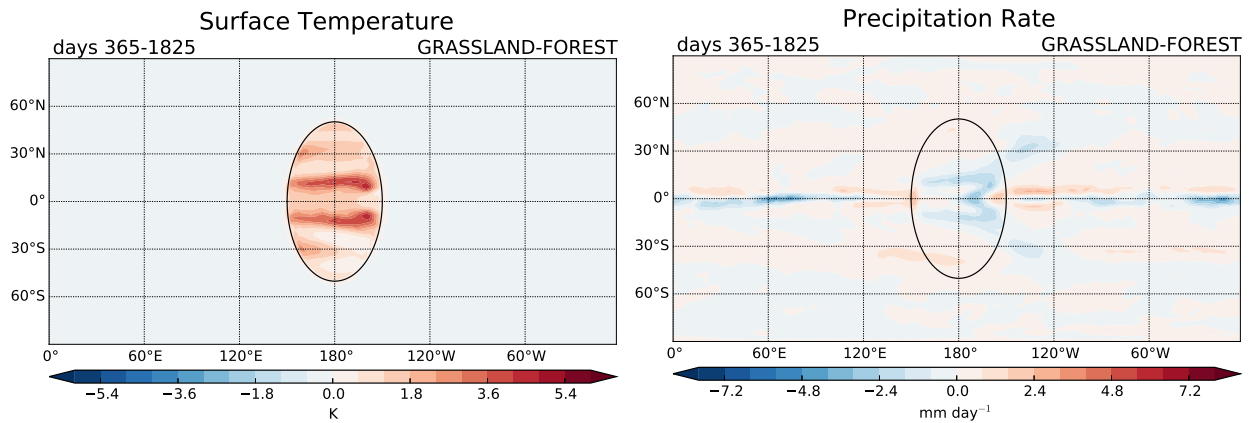
(A) FOREST Temperature

(B) FOREST Precipitation



(C) GRASSLAND Temperature

(D) GRASSLAND Precipitation



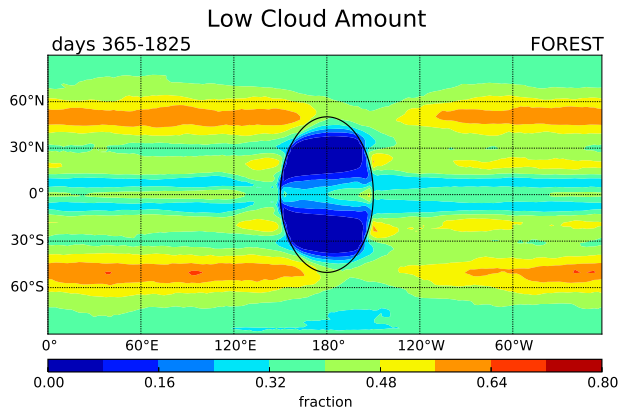
(E) Temperature Difference

(F) Precipitation Difference

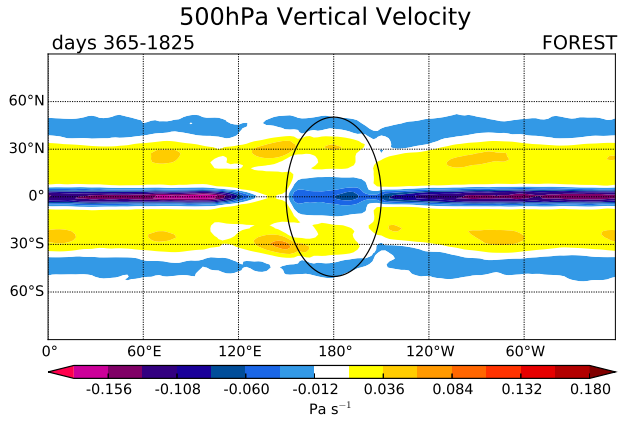
FIGURE 4.1. FOREST, GRASSLAND, and GRASSLAND-FOREST surface temperature (a, c, e) and precipitation rates (b, d, f).

the time averaged (from days 365 to 1,825) surface temperature and rainfall rates. Figures 4.1e and 4.1f show the response of temperature and precipitation over the continent to deforestation (GRASSLAND-FOREST). The conversion of forest to grassland leads to an overall warming over the continent with a maximum warming of about 4.5 Kelvin (Figure 4.1e). We do not see any temperature change over the ocean because SST is prescribed throughout the simulation. The warming over the land mass is accompanied by a decrease in rainfall rate of approximately 1-3 mm day⁻¹ from about 25°N to 25°S. There is also a slight increase in precipitation to the west, and similar increase to the east, of the continent of about 1-2 mm day⁻¹. As discussed in Chapter 1, an increase in precipitation over the eastern Pacific is associated with the El Niño phenomenon. The increase in rainfall to the west of the continent, seen in Figure 4.1f, is possibly a manifestation of an El Niño-like phenomenon. Conversely, the teleconnection maps in Chapter 2 show La Niña conditions (Figure 2.2b) with a decrease in precipitation over the eastern Pacific. A local temperature increase and precipitation decrease is consistent with several previous modeling studies of Amazon deforestation (Nobre et al. 1991; Nobre et al. 2009).

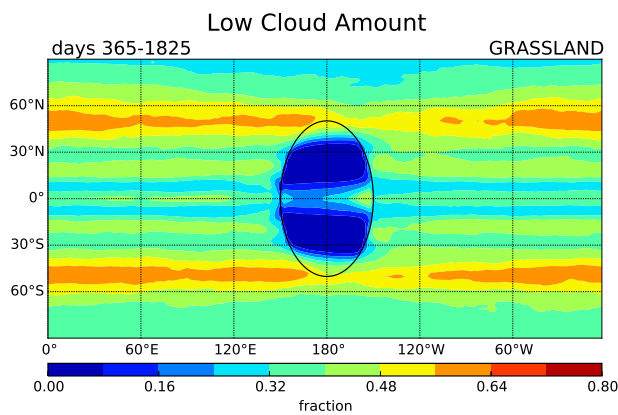
In Chapter 2 we also considered teleconnections between Amazon precipitation and low cloud amount. Marine stratocumulus are prominent over the eastern Pacific during neutral or La Niña conditions of the Walker circulation. During El Niño conditions, when precipitation over the Amazon is reduced, the marine stratocumulus decks over the eastern Pacific are replaced by deep convective clouds as precipitation centers are shifted to the central and eastern Pacific. Low cloud amount and 500 hPa vertical velocity (Pa s⁻¹) are displayed in Figure 4.2. Conversion of forest to grassland in our simulations leads to a decrease in low cloud amount to the west of the continent (Figure 4.2e), which is consistent with



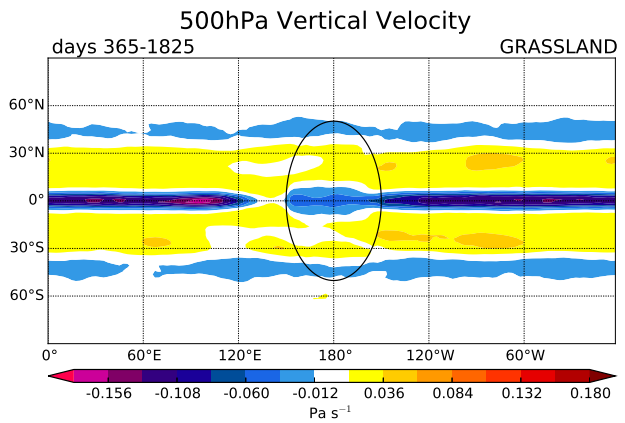
(A) FOREST Low Cloud Amount



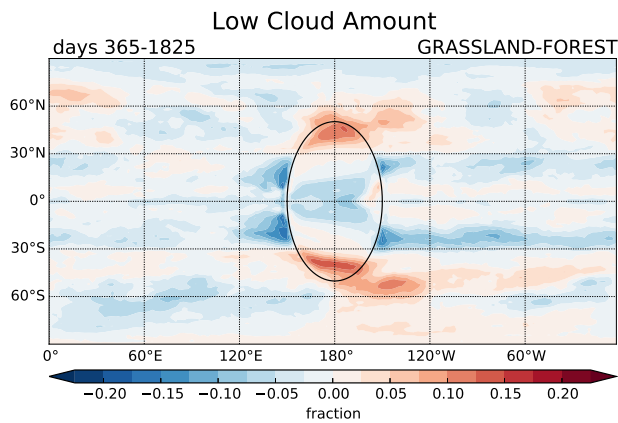
(B) FOREST 500 hPa Vertical Velocity



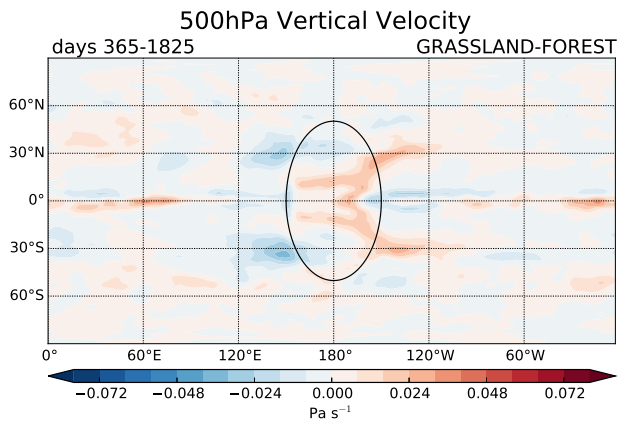
(C) GRASSLAND Low Cloud Amount



(D) GRASSLAND hPa Vertical Velocity



(E) Difference in Low Cloud Amount

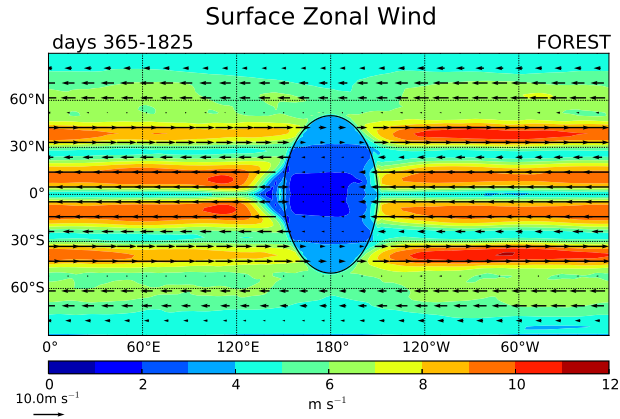


(F) Difference in 500 hPa Vertical Velocity

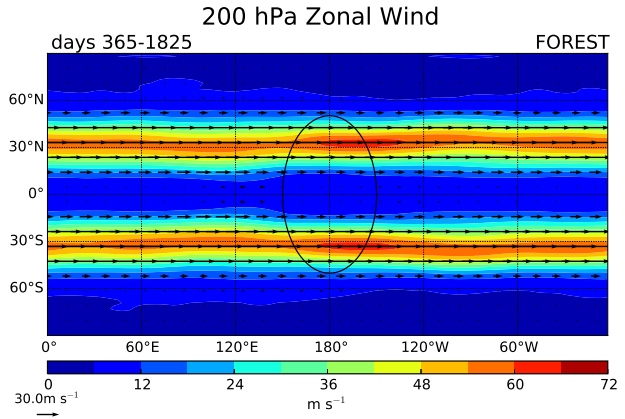
FIGURE 4.2. FOREST, GRASSLAND, and GRASSLAND-FOREST low cloud amount (a, c, e) and 500 hPa vertical velocity (b, d, f).

El Niño conditions and opposite of La Niña conditions (Figure 2.2c). The existence of marine stratocumulus in the eastern Pacific is supported by large scale subsidence that occurs there in the sinking branch of the Walker circulation. The subsidence is supported by convection and rising motion over the Amazon. In our simulations (Figures 4.2b and 4.2d) we get rising motion near the equator over the land mass as well as along the equator over the ocean (blue colors) except for the region just west the continent, which shows sinking motion (warm, yellow contours). There is also broad a broad region of sinking motion over the subtropics seen in the figures. The difference in mid-level vertical motion between the GRASSLAND and FOREST simulations is presented in (Figure 4.2f). The positive difference (red contours) over the tropical land mass are interpreted as a decrease in convection and negative numbers (blue contours) to the west of the continent illustrate a decrease in sinking motion. Figure 4.2f illustrates that deforestation over the continent leads to decreased convection over the deforested region and decreased subsidence to the west of continent. As expected, the difference in 500 hPa vertical velocity looks opposite the effect we see over the eastern Pacific and South America in the teleconnection map in Chapter 2 (Figure 2.2d).

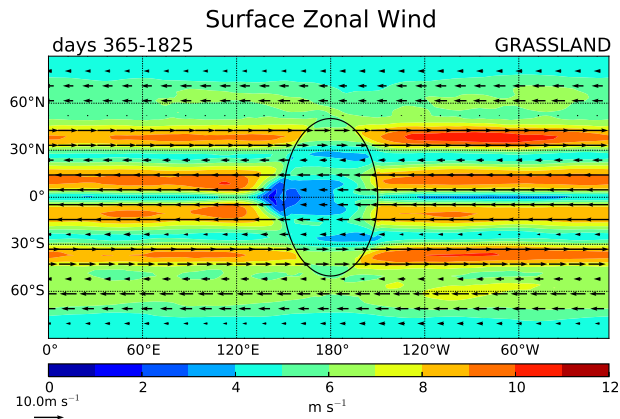
We can investigate the impact of forest conversion to grassland on the “Walker” circulation in our model by looking at the zonal surface and upper tropospheric wind. As in the real-world Walker circulation, we see surface easterlies near the equator (Figure 4.3a) and a very weak westerly return flow in the upper troposphere at 200 hPa (Figure 4.3b). We expect the surface winds over the continent to become stronger due to the decreased surface roughness of the grassland. This change can be seen comparing the zonal wind speed over land in Figures 4.3a and 4.3c. The red contours to the west of the continent in Figure 4.3e illustrate that



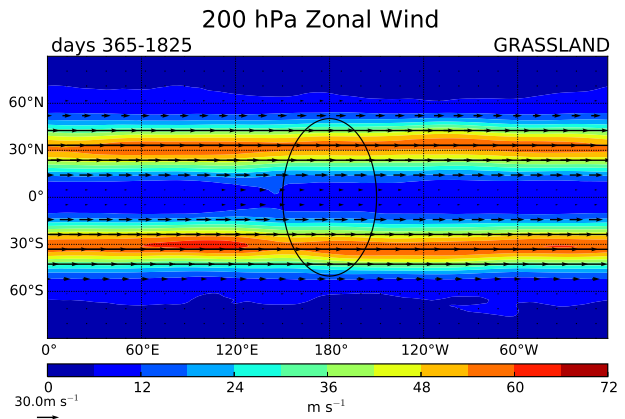
(A) FOREST Surface Zonal Wind



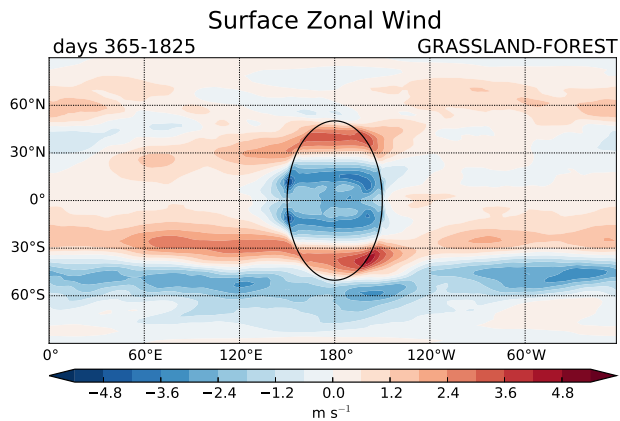
(B) FOREST 200 hPa Zonal Wind



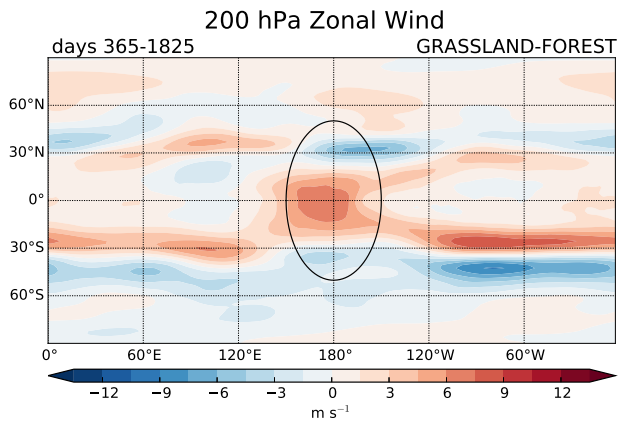
(C) GRASSLAND Surface Zonal Wind



(D) GRASSLAND 200 hPa Zonal Wind



(E) Difference in Surface Zonal Wind

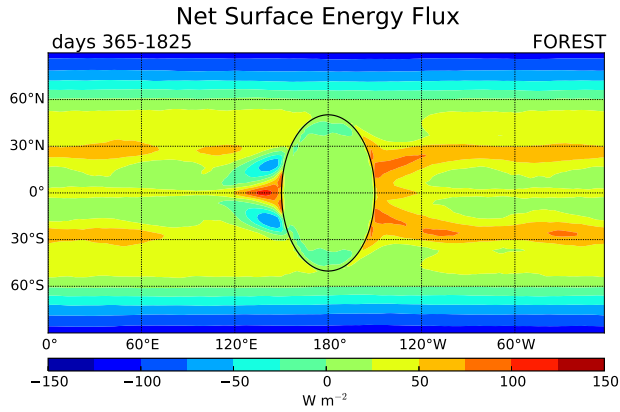


(F) Difference in 200 hPa Zonal Wind

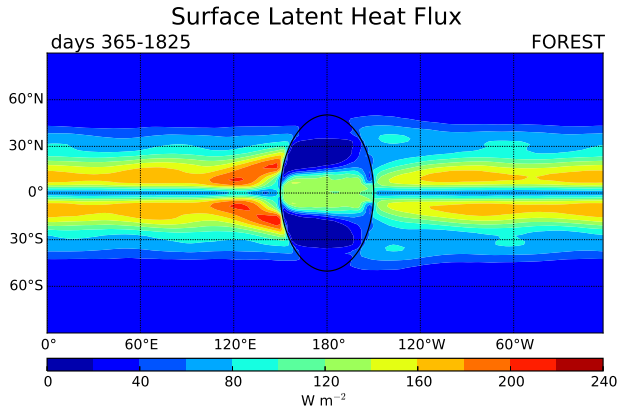
FIGURE 4.3. FOREST, GRASSLAND, and GRASSLAND-FOREST surface zonal wind (a, c, e) and 200 hPa zonal wind (b, d, f). The difference plot contours show the change in direction of the zonal wind. Red contours are a decrease in westerlies and blue contours a decrease in easterlies (e, f).

the easterly surface zonal wind decreases in the GRASSLAND run (becomes more westerly) by about 1 m s^{-1} . A weakening of the easterly surface winds indicates a weakening of the circulation to the west of the continent. The 200 hPa zonal wind difference (Figure 4.3f) shows that the upper tropospheric zonal wind becomes slightly more easterly (blue contours) by about 0.5 m s^{-1} . We expect a decrease in upper tropospheric zonal wind, and although we see one in our simulations, it is very weak. The return flow at 200 hPa in our simulations are much weaker than the observations show.

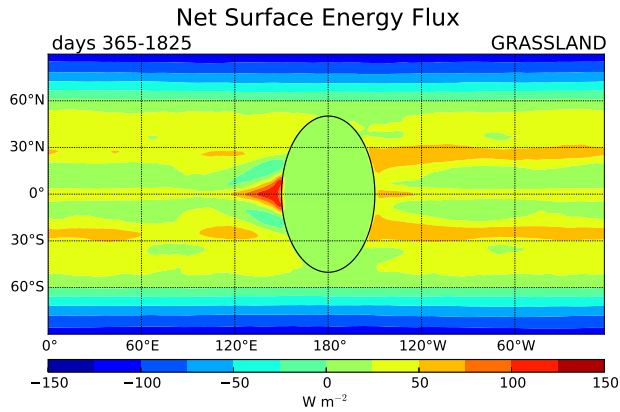
We can also take a look at the net surface energy flux to get an idea of how the ocean will respond to the change in vegetation over the continent (Figure 4.4). Although the SST is prescribed in our simulations, the net surface energy flux is a good indicator of how ocean temperatures may respond. The net surface energy flux is the sum of the net radiative (solar and longwave) and turbulence (sensible and latent heat) fluxes. Figure 4.4e shows the difference between the net surface energy flux between the GRASSLAND and FOREST simulations. The red contours to the west of the continent indicate an increased downward net flux of energy to the surface by about 40 W m^{-2} . East of the continent we get a proportional decrease in net surface energy flux. The net surface energy flux difference suggests that the SST will increase to the west of the continent and cool to the east of the continent in the GRASSLAND simulation. As we have discussed, warm SSTs in the eastern Pacific are a characteristic of an El Niño. This result implies that deforestation over the continent could result in warmer SST to the west of the continent, and reinforce an El Niño. The net surface energy flux is nearly zero over the land because we have averaged over a long time period and the ground stores very little heat.



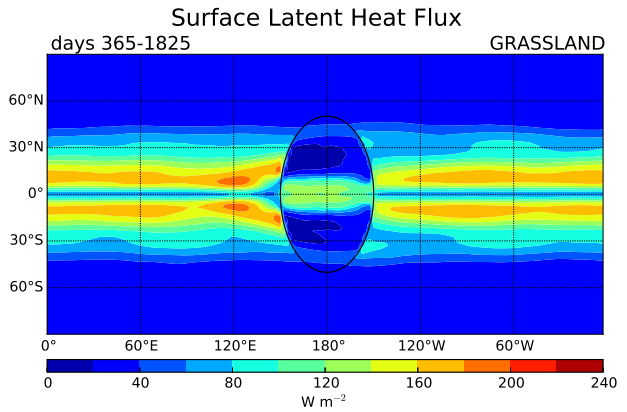
(A) FOREST Net Surface Energy Flux



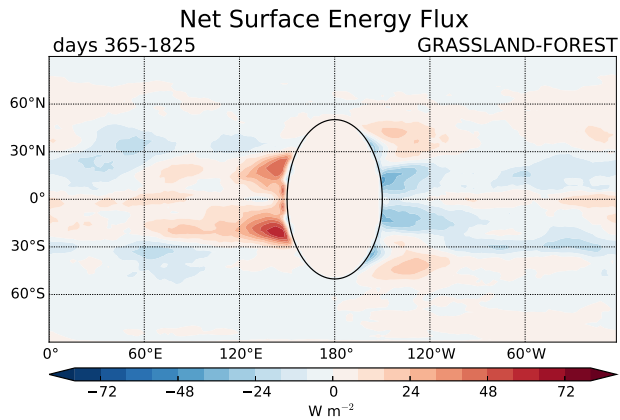
(B) FOREST Surface Latent Heat Flux



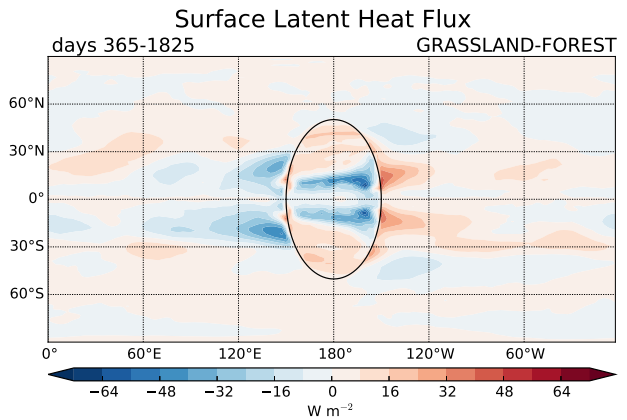
(C) GRASSLAND Net Surface Energy Flux



(D) GRASSLAND Surface Latent Heat Flux



(E) Net Surface Energy Flux Difference



(F) Surface Latent Heat Flux Difference

FIGURE 4.4. FOREST, GRASSLAND and GRASSLAND-FOREST net surface energy balance (a, c, e) and surface latent heat flux (b, d, f).

The largest contribution to the net surface energy flux difference between the GRASSLAND and FOREST simulations is the net surface latent heat flux (Figure 4.4f), which accounts for roughly half of the difference. The upward surface latent heat flux decreased to the west of the continent in the GRASSLAND simulation. Part of this decrease in surface latent heat flux can be explained by the decrease in surface wind speed (Figure 4.3e) at roughly the same locations (just north and south of the equator to the west of the continent) as the decrease in the surface latent heat flux (Figure 4.4f). A weakening of the surface winds over the ocean would mean a decrease in evaporation and consequently a decrease in latent heat flux. Another contribution to the increase in net downward surface energy to the west of the continent is the increase in net downward solar flux (not shown), which is due to a decrease in low cloud amount (Figure 4.2e) as well as total cloud amount (not shown).

4.2. SIMULATIONS WITH TOPOGRAPHY

We are also interested in the role that the Andes play in the coupling of vegetation and precipitation over South America to the eastern Pacific. The Andes have implications for surface winds and moisture transport to the Amazon rainforest, which further impact rainfall rates over tropical South America. We added an idealized mountain range with a similar geometry to the Andes to our idealized set-up.

Overall the simulations with the addition of the Andes-like mountain range look very similar to the basic idealized set-up. We still see strong warming over the continent, with the exception of a few regions in the higher latitudes that show cooling (Figure 4.5a). We also see a broad region of decreased precipitation between about 25°N and 25°S, but there is also a small region of increase in the center of the continent (Figure 4.5b). The increase

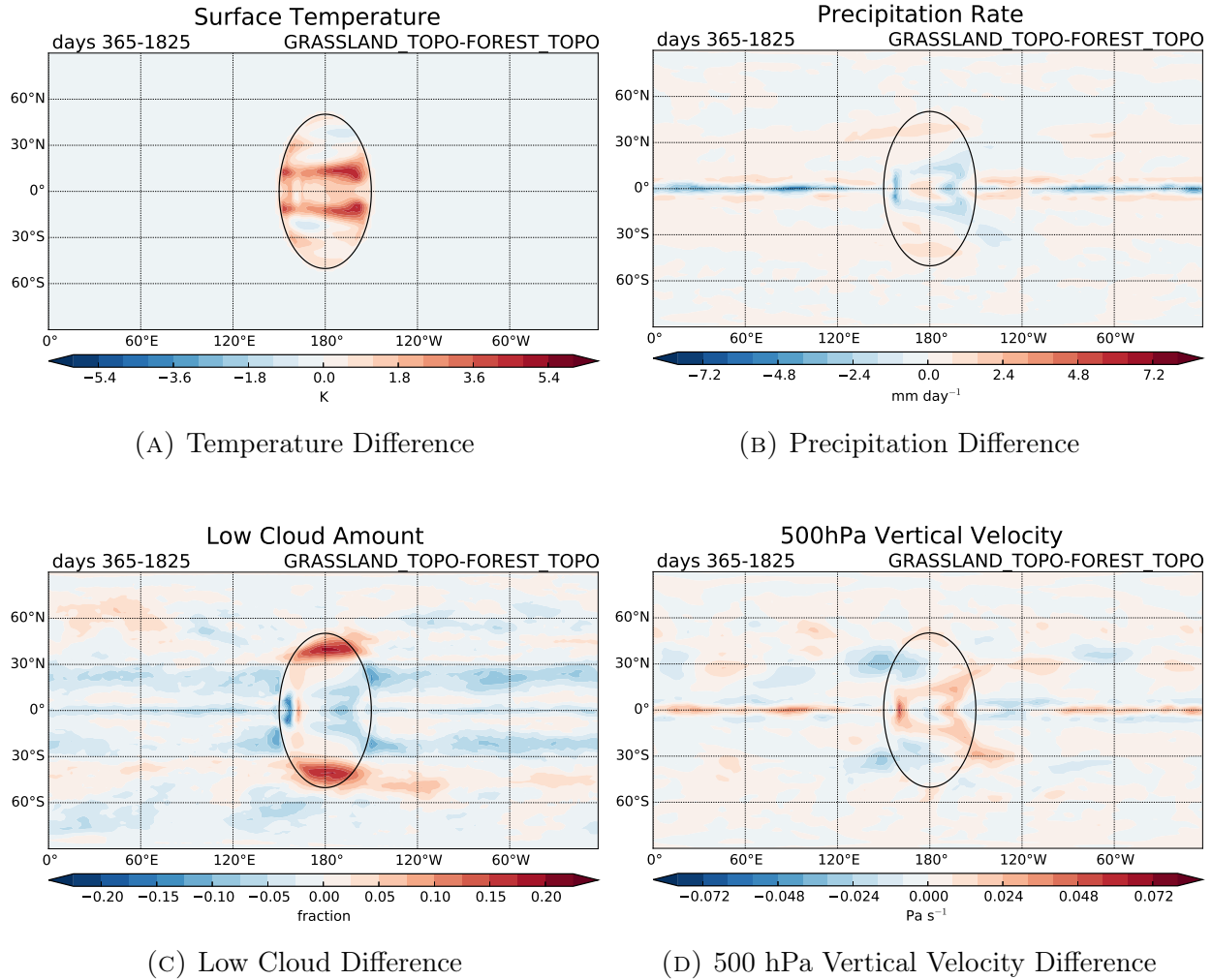


FIGURE 4.5. Difference plots (GRASSLAND_TOPO-FOREST_TOPO) for (a) surface temperature (b) precipitation rate, (c) low cloud amount, and (d) 500 hPa vertical velocity.

rainfall rate in the center of the continent is probably due to the combination of increased wind speed over land and as a result increased convection forced by the topography. We also see an increase in precipitation to the west of the continent (Figure 4.5b) of about the same magnitude as the simulations with the basic set-up. As expected, low cloud amount decreases to the west of the continent (Figure 4.5c), where we expect low clouds to be replaced by deep convection. There is also increased subsidence over the continent (Figure 4.5d), consistent with the previous simulations.

We see a similar response in the surface and 200 hPa zonal winds to the baseline simulations when we add the mountain range (Figures 4.6a and 4.6b). We see a slight westerly increase in the zonal surface wind (decrease in surface easterlies) to the west of the continent and a very weak change in the zonal wind at the 200 hPa level. The increase in downward net surface energy flux to the west of the continent is slightly weaker with the addition of the mountain range along the west coast of the continent (Figure 4.6c). This is likely due to the decrease in surface latent heat flux to the west of the continent (Figure 4.6d). The surface latent heat flux west of the continent most likely decreases because the surface winds there are slightly weaker.

4.3. SIMULATIONS WITH A SLAB OCEAN MODEL

In our last set of simulations we added a very simple slab ocean model (SOM) to the idealized set-up. The addition of the slab ocean model allows us to get an idea of how the eastern Pacific SST will respond to deforestation over South America. The previous simulations suggested that the ocean to the west of the continent will warm and cool to the east of the continent based on the downward net surface energy flux to the surface. With the added slab ocean model we see a maximum warming to the west of the continent of about 1°C (Figure 4.7a). For comparison, during an El Niño the average warming of the eastern Pacific is about $0.5\text{-}2^{\circ}\text{C}$ above average (Trenberth 1997). We also see strong warming over the land from 25°N to 25°S with a maximum of about 6.5°C . Unlike the other simulations, the experiments with the slab ocean model show mostly cooling in the higher latitudes over the land mass. We also see cooler SSTs to the east of the continent in response to deforestation. The ocean to the east of the continent could possibly be compared to the

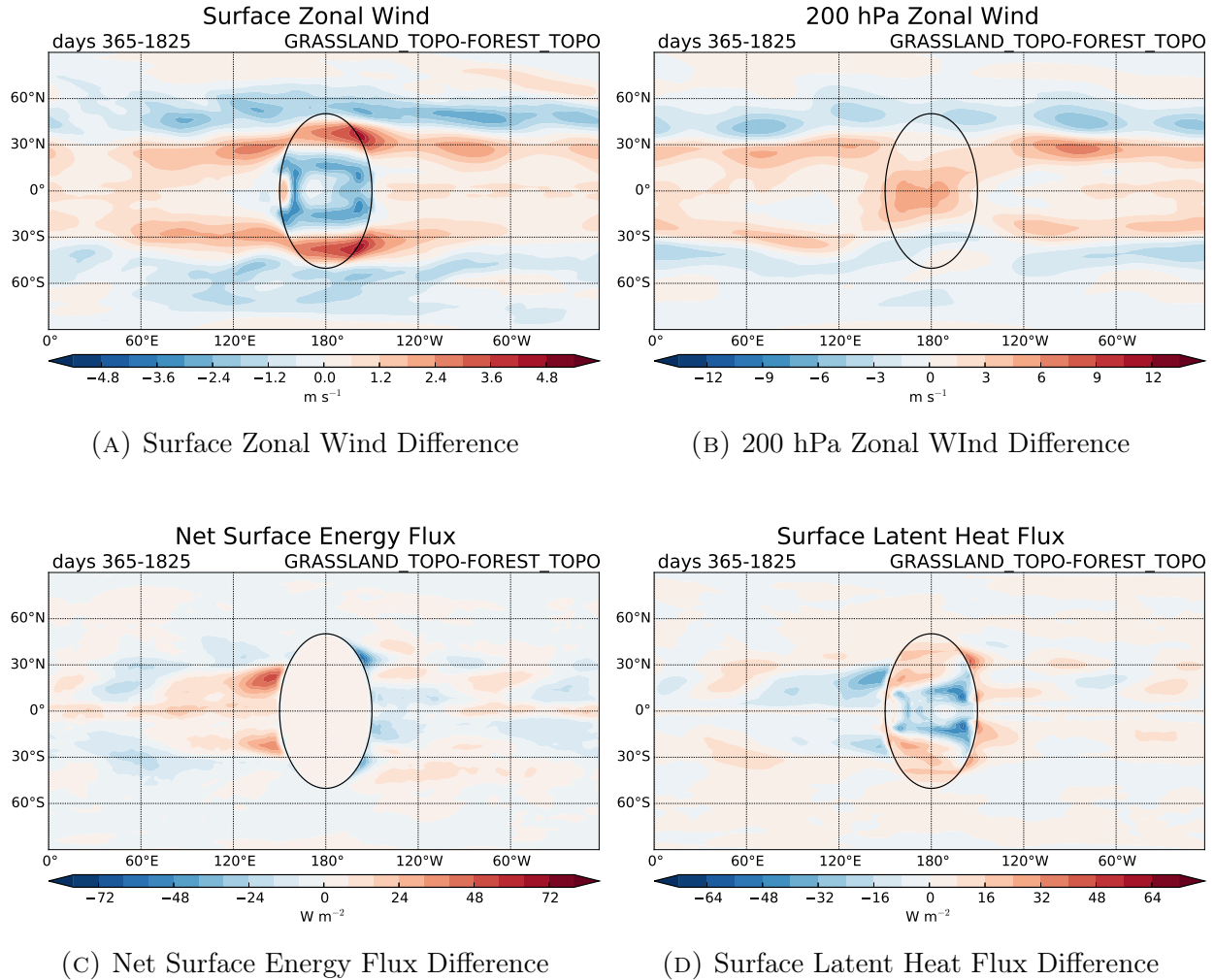


FIGURE 4.6. Difference plots (GRASSLAND_TOPO-FOREST_TOPO) for (a) surface zonal wind (b) 200 hPa zonal wind, (c) net surface energy flux, and (d) surface latent heat flux.

Atlantic. Atlantic SSTs also have an impact on Amazonian precipitation, as discussed in Chapter 1. McGregor et al. (2014) were able to link Walker circulation intensification to warming in the Atlantic. They found that Atlantic warming led to upward motion over the Atlantic region and sinking motion over the central and eastern equatorial Pacific. It is possible that Atlantic cooling, like we see in our simulations, could also contribute to a weakening of the Walker circulation by causing descending motion over the Atlantic (east of

the continent) and enhancing upward motion over the central and eastern Pacific (west of the continent).

The decrease in precipitation over land for the SOM simulations has a similar shape and magnitude to the precipitation decrease in the baseline experiments, with the exception of precipitation to the east of the continent. The simulations with prescribed SST showed an increase in precipitation to the east of the continents as well, but here with the slab ocean model we see that precipitation decreases to the east of the continent. Precipitation to the west of the continent increased the most in these simulations (Figure 4.7b) with a maximum increase of about 5 mm day^{-1} . An increase in SST and rainfall to the west of the continent is an indication of an El Niño-like phenomenon, the response we expect from large-scale deforestation.

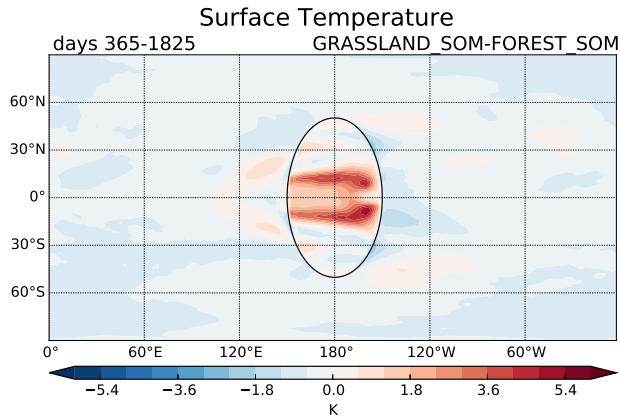
The warm waters welcome deep convection, and the low marine stratocumulus clouds that usually accompany the cold waters in the eastern Pacific are replaced by deeper clouds during an El Niño. This is what we see in our simulations with the slab ocean model. Allowing the SST to vary, results in warming east of the continent which results in decreased low cloud amount there (Figure 4.7c). The increase in deep convection is reflected in the 500 hPa vertical velocity where we see a decrease in sinking motion to the west of the continent and an increase in subsidence over the continent and east of the continent where precipitation decreases (Figure 4.7d).

The effect of deforestation on the “Walker” circulation in our SOM simulations is clearer and stronger than the previous simulations. The easterly surface zonal wind along the equator west of the continent clearly decreases (become more westerly) as depicted by the red contours in response to the deforestation (Figure 4.7e). Similarly, the westerly 200 hPa

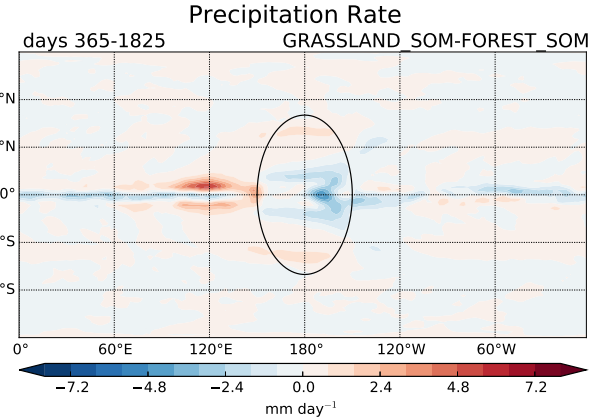
zonal wind decrease west of the continent near the equator (Figure 4.7f). The addition of the coupled slab ocean model was important in affecting the strength of the Walker circulation. Nobre et al. (2009), also found that the inclusion of a coupled ocean model enhanced rainfall reductions and surface warming over the deforested region compared to the simulations without the couple ocean. They also found that the coupled ocean model was important for interpreting remote responses to deforestation, such as over the eastern Pacific. The results from the slab ocean model simulations exhibited the behavior we expected in response to deforestation. This simulation consistently met our expectations, which highlights the importance of a coupled ocean in determining large scale response to deforestation.

4.4. SIMULATIONS WITH SP-CAM

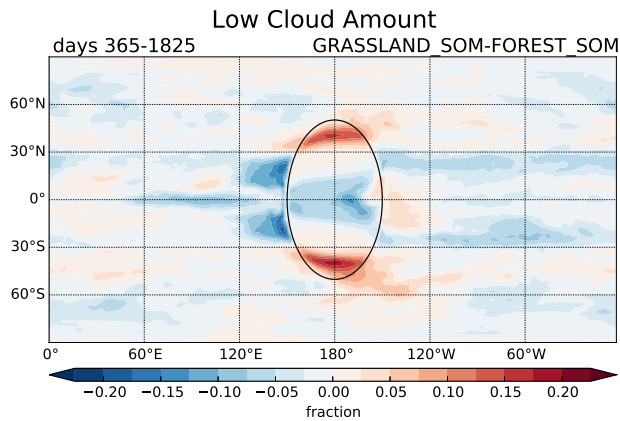
Clouds and precipitation are calculated in a completely different way in the SP-CAM. As discussed previously, a two-dimensional CRM is embedded within each grid cell of the GCM. We repeated the FOREST and GRASSLAND simulations using the SP-CAM (FOREST_SP and GRASSLAND_SP). Both the FOREST_SP and GRASSLAND_SP simulations are warmer than their respective counterparts based on the conventional CAM. The temperature difference between the two simulations (GRASSLAND_SP-FOREST_SP) is also stronger and more concentrated towards the center of the continent than with the conventional CAM (Figure 4.8a). The precipitation response is much weaker with SP-CAM than it was with CAM. With SP-CAM we see less precipitation concentrated in a narrower region (latitudinally) over the continent. The precipitation difference (GRASSLAND_SP-FOREST_SP) shows a very weak decrease over the continent and a decrease rather than an increase in precipitation to the west of the continent (Figure 4.8b). When looking at the



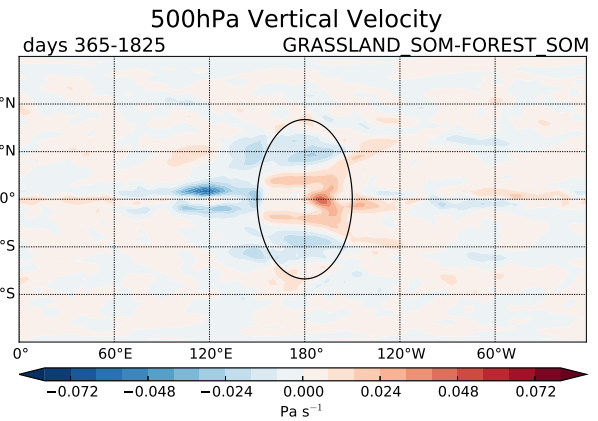
(A) Temperature Difference



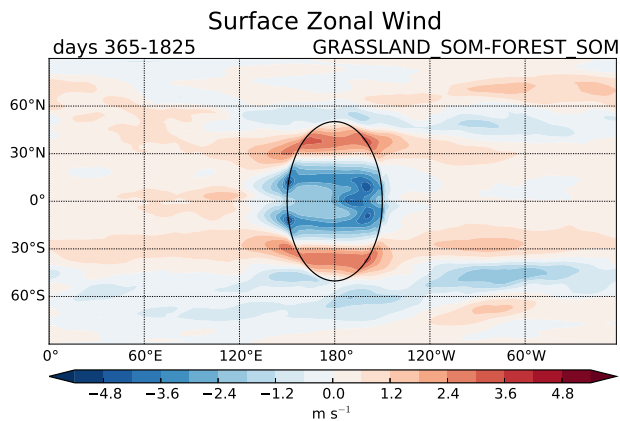
(B) Precipitation Difference



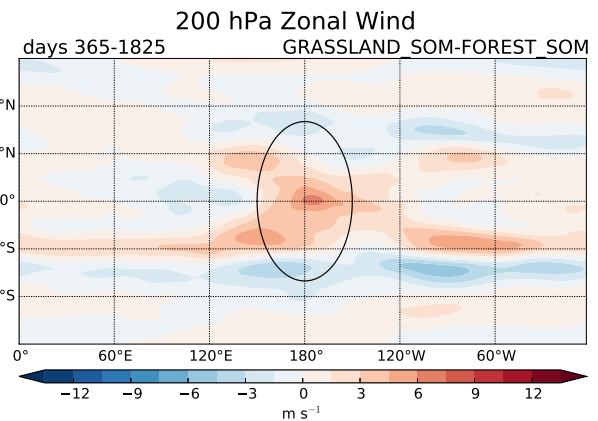
(C) Low Cloud Amount Difference



(D) 500 hPa Vertical Velocity Difference



(E) Surface Zonal Wind Difference



(F) 200 hPa Zonal Wind Difference

FIGURE 4.7. Difference plots (GRASSLAND_SOM-FORSET_SOM) for simulations with slab ocean model for (a) surface temperature, (b) precipitation rate, (c) low cloud amount, (d) 500 hPa vertical velocity, (e) surface zonal wind, and (f) 200 hPa zonal wind.

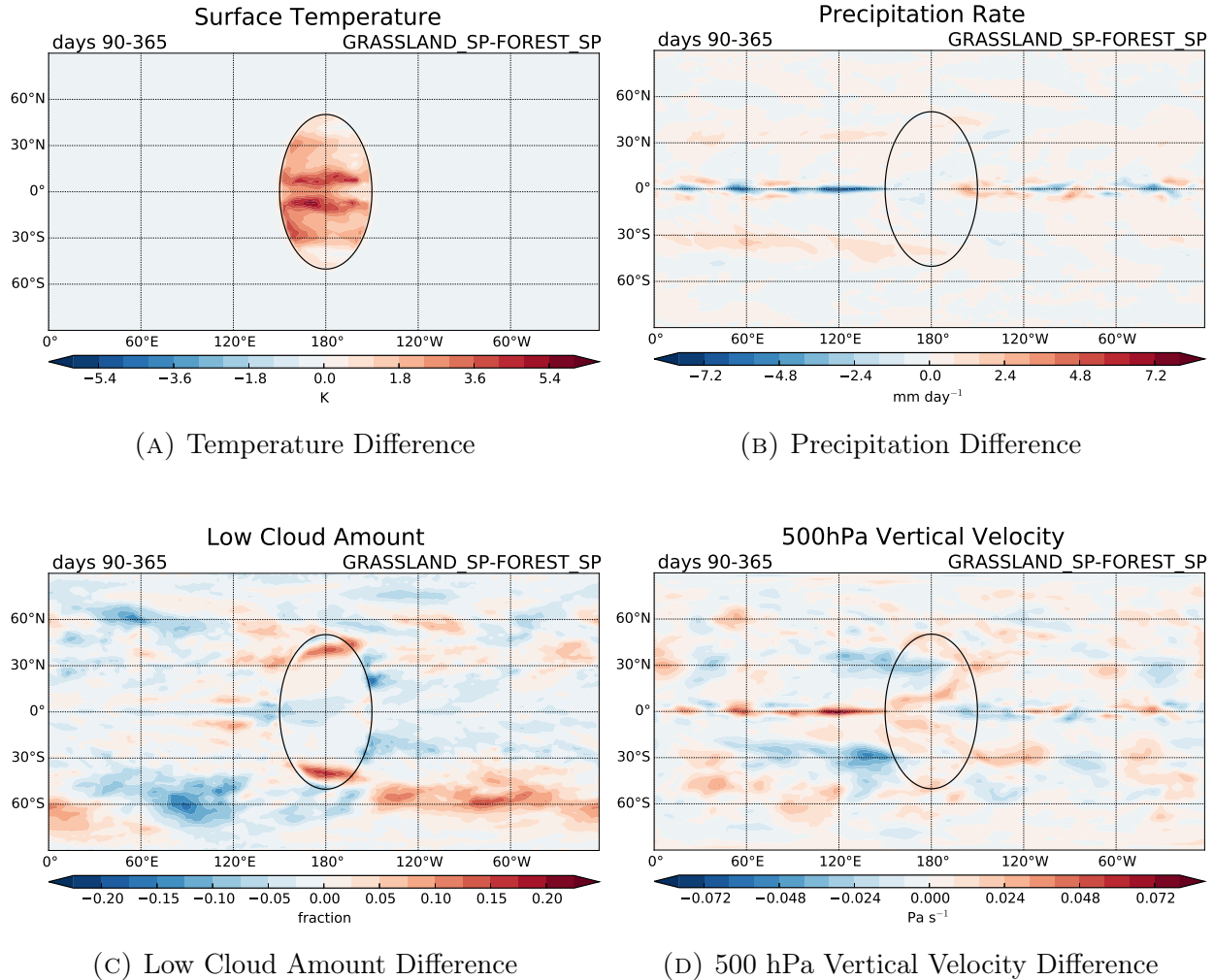


FIGURE 4.8. Difference plots (GRASSLAND_SP-FOREST_SP) for (a) surface temperature (b) precipitation rate, (c) low cloud amount, and (d) 500 hPa vertical velocity.

diurnal cycle of precipitation (Figure 4.9) it is evident that the SP-CAM simulations have significantly less precipitation than the runs with standard CAM. Another notable difference is the shift in the time of day of the precipitation maximum. The SP-CAM simulations show precipitation peaking in the late afternoon, whereas rainfall in the standard CAM runs peak near noon.

The overall low cloud amount in SP-CAM is lower than in the simulations with the conventional CAM. We expect a decrease in low clouds to the west of the continent, which

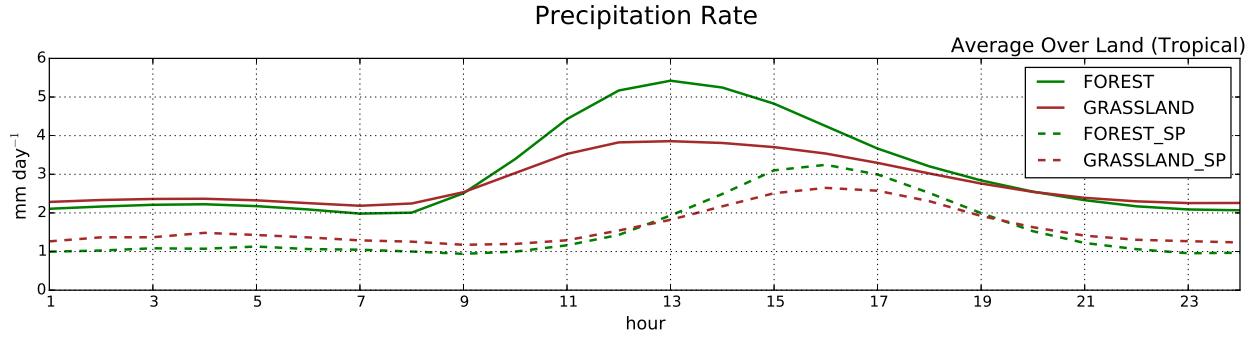


FIGURE 4.9. Diurnal cycle of precipitation in simulations for basic set-up (solid lines) and SP-CAM runs (dashed lines). Green lines are simulations with continent covered in forest and brown lines represent simulations covered in grassland.

is what we saw in the GRASSLAND-FOREST simulation (Figure 4.2e), but for SP we do not get the same response to the west of the continent. In the SP simulations we see a small region of decrease directly to the west of the continent and an increase a little further off the coast of the continent (Figure 4.8c). We do still see decreased convection (more subsidence) over the continent as we expect (Figure 4.8d), but to the west of the continent we also see enhanced subsidence where we expect more convection to correspond to the displaced convection that occurs during an El Niño.

We also get very unclear responses to deforestation in the surface and 200 hPa zonal winds. A decrease in the strength of the Walker circulation and hence the surface and 200 hPa zonal winds is expected in response to deforestation, but for our simulations with the SP-CAM we see a mixed signal. The surface zonal wind shows a very weak change near the equator to the west of the continent (Figure 4.10a) and the westerly 200 hPa zonal wind slightly increased to the west of the continent (Figure 4.10b).

The difference between the two simulations for SP (GRASSLAND_SP-FOREST_SP) for the net surface energy flux (Figure 4.10c) gives the expected response. An increase in

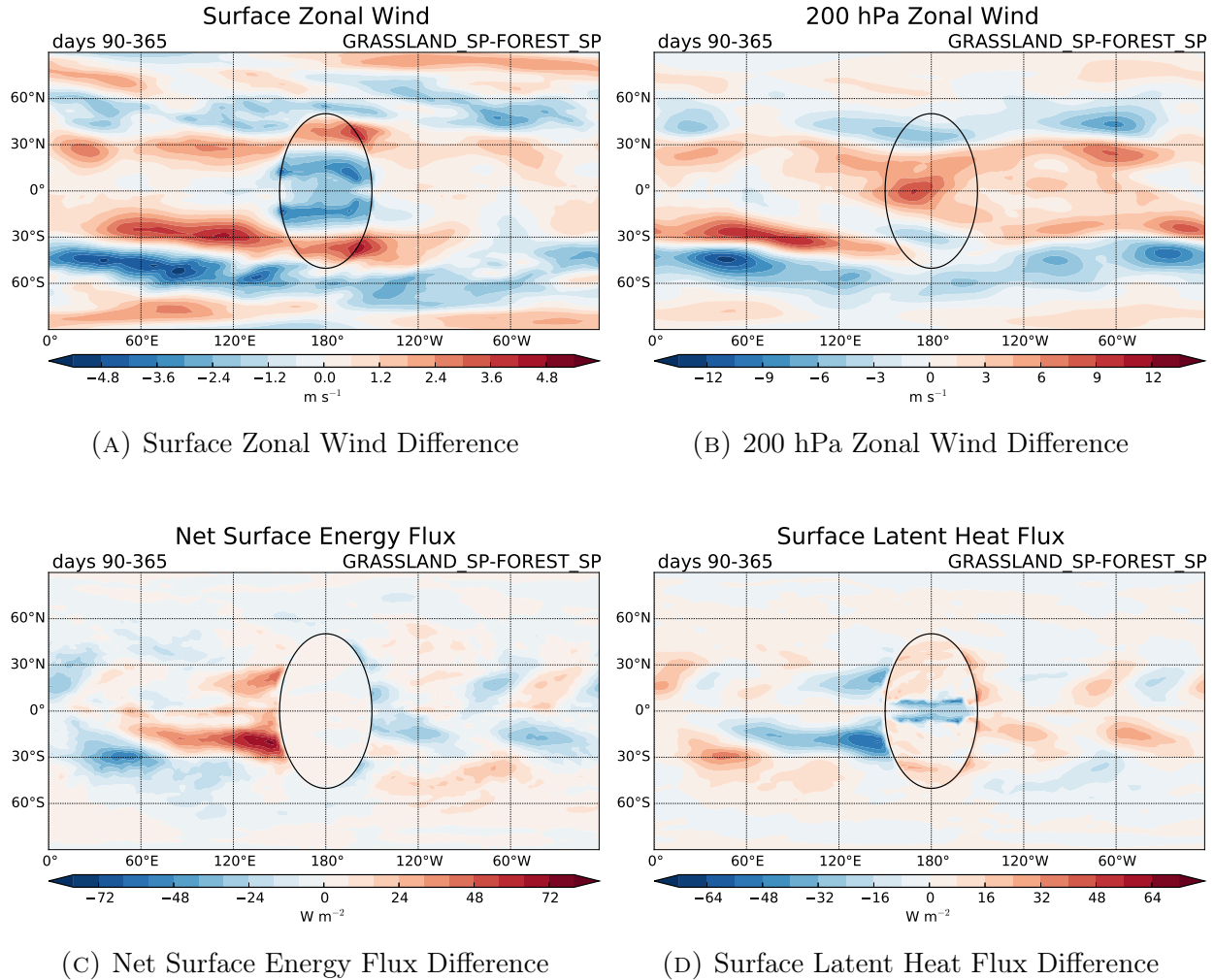


FIGURE 4.10. Difference plots (GRASSLAND_SP-FOREST_SP) for (a) surface zonal wind (b) 200 hPa zonal wind, (c) net surface energy flux, and (d) surface latent heat flux.

downward net surface energy flux to the west of the continent, again, implies that the surface will warm there. The strength and span of this increase in net downward surface energy flux is greater for the SP runs (Figure 4.10c) than it was previously for the simulations with standard CAM (Figure 4.4e). Again, the largest contributor to this surface energy flux is the change in surface latent heat flux (Figure 4.10d).

Although the response of precipitation, low cloud amount, and the strength of the Walker circulation was opposite of what we expected for these simulations, we do still see significant

warming over the land and an indication that the ocean to the west of the continent will also warm. The drastic differences between the simulations that used the standard CAM and those that used the SP-CAM could be due to not enough spin-up time for the model. The SP-CAM simulations were only run for 365 days as opposed to the 1,825 days for those which used the conventional CAM. The initial conditions were also different for simulations with the SP-CAM. We branched the SP-CAM simulations from the end of the baseline simulations. It is possible that this also had impacts on the evolution of the SP-CAM simulations.

CHAPTER 5

CONCLUSIONS

5.1. SUMMARY AND DISCUSSION

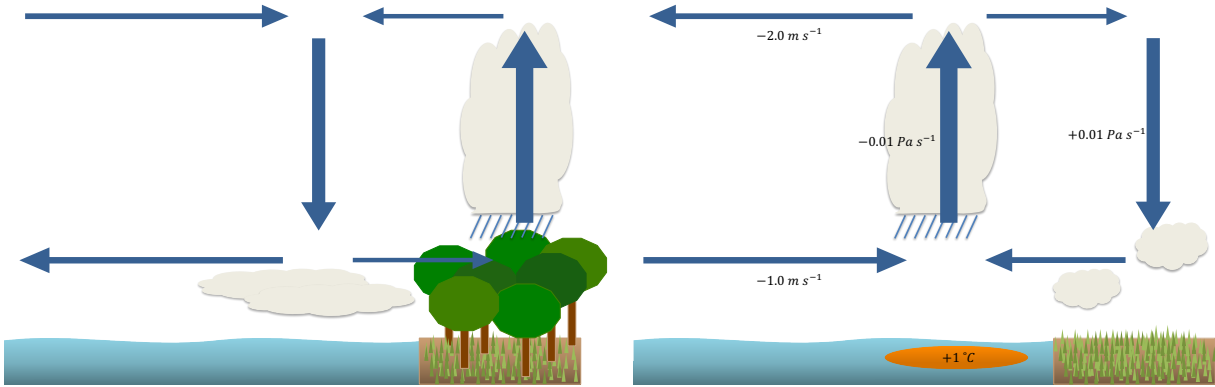
The Amazon rainforest is threatened by many factors including climate change and clearing for agricultural reasons. Forest fires and dieback are more likely due to increased frequency and intensity of droughts in the region. It is possible that extensive Amazon deforestation can induce an El Niño like state. The conversion of forest to grassland has implications for precipitation and vertical motion over the region and can impact the larger Walker circulation via the increased subsidence that occurs over tropical South America. The global impact of large-scale Amazon deforestation was investigated using a global atmospheric model (CAM4) coupled to a land model (CLM4) to simulate an idealized planet with a continent initially covered in forest then, in a separate simulation, covered in grassland. These baseline simulations were repeated three times with: 1) an Andes-like mountain range, 2) a simple slab ocean model, and 3) the conventional CAM replaced with the SP-CAM. The continent in our simulations was compared to the Amazon and the ocean to the west of the continent was compared to the eastern Pacific.

5.1.1. CONVENTIONAL CAM SIMULATIONS. The baseline simulations, which used the conventional CAM, prescribed SST, and flat topography, gave the expected response to deforestation over the continent but a weak response over the ocean. Stronger responses over the ocean were obtained with the addition of the slab ocean model. All of the simulations resulted in a broad region of warming of approximately 3-4°C over the continent when forest was converted to grassland. Changes in precipitation were also consistent for simulations

with the conventional CAM, with a decrease over land and an increase over the ocean to the west of the continent, but the magnitudes for the simulations with the slab ocean model were greater. The precipitation decrease over land for the baseline simulations and those with the added mountain range was about 1-3 mm day⁻¹ and the increase to the west of the continent was about 1-2 mm day⁻¹. The corresponding decrease and increase for the simulations with the slab ocean model were 2-4 mm day⁻¹ over land and 3-5 mm day⁻¹ west of the continent.

Our idealized simulations resulted in decreased low cloud amount to the west of the continent by about 10-20%. During an El Niño, the eastern Pacific warms and precipitation centers are shifted to the central and eastern Pacific, where deep convective clouds replace low marine stratocumulus clouds. Although the waters to the west of the continent in our simulation do not warm, the vertical motion there can still be affected by the change in vertical motion caused by the change in vegetation over the continent. A prominent increase in sinking motion was observed over the continent in all of the simulations. A change from forest to grassland can enhance subsidence (or suppress convection) via decreased latent heat flux. Latent heat flux is smaller over a grassland than a forest partly due to the decreased evapotranspiration over a grassland. The decrease in latent heat flux limits the upward vertical motion that occurs and leads to a decrease in convection.

The Walker circulation was expected to weaken in response to Amazon deforestation, which was observed in the surface and 200 hPa winds for all of the simulations with the conventional CAM. A schematic showing the differences in circulations between the simulations with forest and those with grassland is illustrated in Figure 5.1. For the simulations with the land covered in forest deep convection and precipitation are strong over the land, subsidence



(A) Forest Simulations

(B) Grassland Simulations

FIGURE 5.1. Schematic of circulation in simulations with (a) forest and (b) grassland.

and low marine stratocumulus are prominent west of the continent over the ocean, and surface easterlies paired with upper tropospheric westerly winds exist (Figure 5.1a). When the forest is converted to grassland convection is suppressed over the land, deep convection and precipitation occur west of the continent over a region of anomalously warm SST ($\sim 1^\circ\text{C}$), and surface easterlies decrease by about 1 m s^{-1} while upper tropospheric westerlies decrease by about 2 m s^{-1} (Figure 5.1b).

Because the sea surface temperature was prescribed, we expected an imbalance in the net surface energy flux. This imbalance gave us an idea of how SSTs would respond in a simulation with a coupled ocean. All of the simulations with prescribed SST indicated that the surface water to the west of the continent would warm, which is what we saw when we added the slab ocean model. The largest contributor to the increased downward net surface energy flux to the west of the continent was the decrease in upward latent heat flux there. This was likely due to decreased surface wind speed and therefore decreased evaporation west of the continent.

Adding the idealized mountain range did not seem to have very significant impacts when compared to the baseline simulations with flat topography. Adding the slab ocean model appeared to have the greatest impact on the magnitude of the changes obtained in the baseline simulations. The addition of the slab ocean model revealed that SST to the west of the continent increased by about 0.5-1°C in response to deforestation. This result suggests that deforestation is indeed capable of altering the SST in surrounding oceans. In addition to the warming of the ocean to the west of the continent, the atmosphere also exhibited several other El Niño-like characteristics. Precipitation increased west of the continent alongside a decrease in low cloud amount. A prominent feature of El Niño is the shifting of precipitation centers from the west to the central and eastern Pacific. Another notable result of the simulations with the included slab ocean model was the response of the “Walker” circulation. The Walker circulation decreases during an El Niño, which is what allows the SSTs in the eastern Pacific to warm. An obvious decrease in surface and 200 hPa winds was observed in our simulations. The slab ocean model proved to be important for getting the expected response in the Walker circulation west of the continent. The results presented here suggest that large-scale deforestation can significantly impact global circulations and potentially enhance El Niño conditions. The role of a coupled ocean model was also found to be of great importance in determining global impacts of deforestation.

5.1.2. SP-CAM SIMULATIONS. Our results for the simulations with SP-CAM were a little more mixed than those with the conventional CAM. In the SP-CAM simulations, only a very weak decrease in precipitation resulted from the deforestation, although we did see slightly greater warming over the continent. The precipitation change to the west of the continent was also opposite the other simulations for the SP-CAM simulation, where instead

of the expected increase, we saw a decrease in a narrow band along the equator. The change in low cloud amount to the west of the continent was also different than the previous simulations with the conventional CAM. Rather than a decrease we saw a mixed response with areas of decrease and increase west of the continent. The change in the “Walker” circulation (surface and 200 hPa winds) was also opposite of what we expected with increases in zonal wind, rather than decreases. It is possible that the reason we do not see the expected changes in the SP-CAM is because we did not allow sufficient time for the model to adjust, despite our intention of shortening the needed spin-up time by branching the SP-CAM simulations from the end of the conventional CAM simulations. We only ran these simulations for 365 days compared to 1,825 days for the simulations with the conventional CAM.

5.2. FUTURE WORK

The idealized simulations in this study strongly suggest that Amazon deforestation can impact the Walker circulation and induce an El Niño. We would like to further investigate these simulations with the SP-CAM to see if running the simulations longer and allowing more time for the model to adjust will change the results. We suspect that doing a startup run (rather than branching from the end of the conventional CAM simulations) and running for an equal amount of time will give us the expected results. Because the slab ocean model appeared to be of great importance in our simulations we would also like to include SP-CAM simulations coupled to a slab ocean.

Whether or not these results would carry over to the real world is still in question. It would be useful to repeat these experiments in “real world” simulations where the Amazon rainforest is replaced with grassland to see if an El Niño characteristics can be achieved

as a result of the deforestation. Future work could also include experiments with dynamic vegetation where forest is converted to grassland and then back to forest over a period of time in order to investigate how long it takes the atmosphere to respond.

REFERENCES

- Adler, R. F., G. J. Huffman, A. Chang, R. Ferraro, P.-P. Xie, J. Janowiak, B. Rudolf, U. Schneider, S. Curtis, D. Bolvin, A. Gruber, J. Susskind, P. Arkin, and E. Nelkin (2003, 2016/02/12). The Version-2 Global Precipitation Climatology Project (GPCP) Monthly Precipitation Analysis (1979–Present). *Journal of Hydrometeorology* 4(6), 1147–1167.
- Alexander, M. A., I. Bladé, M. Newman, J. R. Lanzante, N.-C. Lau, and J. D. Scott (2002). The Atmospheric Bridge: The Influence of ENSO Teleconnections on Air–Sea Interaction over the Global Oceans. *Journal of Climate* 15(16), 2205–2231.
- Bagley, J. E., A. R. Desai, K. J. Harding, P. K. Snyder, and J. A. Foley (2014, 2015/12/17). Drought and Deforestation: Has Land Cover Change Influenced Recent Precipitation Extremes in the Amazon? *Journal of Climate* 27(1), 345–361.
- Bonan, G. B. (2008). Forests and Climate Change: Forcings, Feedbacks, and the Climate Benefits of Forests. *Science* 320(5882), 1444–1449.
- Charney, J., W. J. Quirk, S. hsien Chow, and J. Kornfield (1977). A Comparative Study of the Effects of Albedo Change on Drought in Semi–Arid Regions. *Journal of the Atmospheric Sciences* 34(9), 1366–1385.
- D’Almeida, C., C. J. Vörösmarty, G. C. Hurtt, J. A. Marengo, S. L. Dingman, and B. D. Keim (2007). The effects of deforestation on the hydrological cycle in Amazonia: a review on scale and resolution. *International Journal of Climatology* 27(5), 633–647.
- Dee, D. P., S. M. Uppala, A. J. Simmons, P. Berrisford, P. Poli, S. Kobayashi, U. Andrae, M. A. Balmaseda, G. Balsamo, P. Bauer, P. Bechtold, A. C. M. Beljaars, L. van de Berg, J. Bidlot, N. Bormann, C. Delsol, R. Dragani, M. Fuentes, A. J. Geer, L. Haimberger, S. B. Healy, H. Hersbach, E. V. Hólm, L. Isaksen, P. Kállberg, M. Köhler, M. Matricardi,

- A. P. McNally, B. M. Monge-Sanz, J.-J. Morcrette, B.-K. Park, C. Peubey, P. de Rosnay, C. Tavalato, J.-N. Thépaut, and F. Vitart (2011). The ERA-Interim reanalysis: configuration and performance of the data assimilation system. *Quarterly Journal of the Royal Meteorological Society* 137(656), 553–597.
- Dickinson, R. E. and A. Henderson-Sellers (1988). Modelling tropical deforestation: A study of GCM land-surface parametrizations. *Quarterly Journal of the Royal Meteorological Society* 114(480), 439–462.
- Evan, A. T., A. K. Heidinger, and D. J. Vimont (2007). Arguments against a physical long-term trend in global ISCCP cloud amounts. *Geophysical Research Letters* 34(4), n/a–n/a. L04701.
- Fu, R., R. E. Dickinson, M. Chen, and H. Wang (2001, 2015/12/17). How Do Tropical Sea Surface Temperatures Influence the Seasonal Distribution of Precipitation in the Equatorial Amazon? *Journal of Climate* 14(20), 4003–4026.
- Gates, W. L., J. S. Boyle, C. Covey, C. G. Dease, C. M. Doutriaux, R. S. Drach, M. Fiorino, P. J. Gleckler, J. J. Hnilo, S. M. Marlais, T. J. Phillips, G. L. Potter, B. D. Santer, K. R. Sperber, K. E. Taylor, and D. N. Williams (1999). An Overview of the Results of the Atmospheric Model Intercomparison Project (AMIP I). *Bulletin of the American Meteorological Society* 80(1), 29–55.
- Gent, P. R., G. Danabasoglu, L. J. Donner, M. M. Holland, E. C. Hunke, S. R. Jayne, D. M. Lawrence, R. B. Neale, P. J. Rasch, M. Vertenstein, P. H. Worley, Z.-L. Yang, and M. Zhang (2011, 2016/02/29). The Community Climate System Model Version 4. *Journal of Climate* 24(19), 4973–4991.

- Hurrell, J. W., M. M. Holland, P. R. Gent, S. Ghan, J. E. Kay, P. J. Kushner, J. F. Lamarque, W. G. Large, D. Lawrence, K. Lindsay, W. H. Lipscomb, M. C. Long, N. Mahowald, D. R. Marsh, R. B. Neale, P. Rasch, S. Vavrus, M. Vertenstein, D. Bader, W. D. Collins, J. J. Hack, J. Kiehl, and S. Marshall (2013, 2016/03/05). The Community Earth System Model: A Framework for Collaborative Research. *Bulletin of the American Meteorological Society* 94(9), 1339–1360.
- Khairoutdinov, M. F. and D. A. Randall (2001). A cloud resolving model as a cloud parameterization in the NCAR Community Climate System Model: Preliminary results. *Geophysical Research Letters* 28(18), 3617–3620.
- Langenbrunner, B. and J. D. Neelin (2013). Analyzing ENSO Teleconnections in CMIP Models as a Measure of Model Fidelity in Simulating Precipitation. *Journal of Climate* 26(13), 4431–4446.
- Lau, K.-M. and S. Yang (2015). Walker Circulation. In F. Z. Gerald North, John Pyle (Ed.), *Encyclopedia of Atmospheric Sciences (Second Edition)* (Second Edition ed.), Volume 6, pp. 177 – 181. Oxford: Academic Press.
- Lean, J. and D. A. Warrilow (1989, 11). Simulation of the regional climatic impact of Amazon deforestation. *Nature* 342(6248), 411–413.
- Lewis, S. L., P. M. Brando, O. L. Phillips, G. M. F. van der Heijden, and D. Nepstad (2011, 02). The 2010 Amazon Drought. *Science* 331(6017), 554–554.
- Li, W., R. Fu, and R. E. Dickinson (2006). Rainfall and its seasonality over the Amazon in the 21st century as assessed by the coupled models for the IPCC AR4. *Journal of Geophysical Research: Atmospheres* 111(D2), n/a–n/a. D02111.

- Malhi, Y., J. T. Roberts, R. A. Betts, T. J. Killeen, W. Li, and C. A. Nobre (2008, 01). Climate Change, Deforestation, and the Fate of the Amazon. *Science* 319(5860), 169–172.
- Marengo, A. J. (2004). Interdecadal variability and trends of rainfall across the Amazon basin. *Theoretical and Applied Climatology* 78(1), 79–96.
- McGregor, S., A. Timmermann, M. F. Stuecker, M. H. England, M. Merrifield, F.-F. Jin, and Y. Chikamoto (2014, 10). Recent Walker circulation strengthening and Pacific cooling amplified by Atlantic warming. *Nature Clim. Change* 4(10), 888–892.
- Mori, S. A. and G. T. Prance (1987). *The Geophysiology of Amazonia*, Chapter Species Diversity, Phenology, Plant-Animal Interactions, and Their Correlation with Climate, as Illustrated by the Brazil Nut Family (Lecythidaceae), pp. 69–90. New York: Wiley.
- Neale, R. B. and B. J. Hoskins (2000). A standard test for AGCMs including their physical parametrizations: I: the proposal. *Atmospheric Science Letters* 1(2), 101–107.
- Nepstad, D., P. Lefebvre, U. Lopes da Silva, J. Tomasella, P. Schlesinger, L. Solórzano, P. Moutinho, D. Ray, and J. Guerreira Benito (2004). Amazon drought and its implications for forest flammability and tree growth: a basin-wide analysis. *Global Change Biology* 10(5), 704–717.
- Nepstad, D. C., C. R. de Carvalho, E. A. Davidson, P. H. Jipp, P. A. Lefebvre, G. H. Negreiros, E. D. da Silva, T. A. Stone, S. E. Trumbore, and S. Vieira (1994, 12). The role of deep roots in the hydrological and carbon cycles of Amazonian forests and pastures. *Nature* 372(6507), 666–669.
- Nobre, C. A., P. J. Sellers, and J. Shukla (1991). Amazonian Deforestation and Regional Climate Change. *Journal of Climate* 4(10), 957–988.

- Nobre, P., M. Malagutti, D. F. Urbano, R. A. F. de Almeida, and E. Giarolla (2009, 2015/12/18). Amazon Deforestation and Climate Change in a Coupled Model Simulation. *Journal of Climate* 22(21), 5686–5697.
- Nobre, P. and J. Shukla (1996). Variations of Sea Surface Temperature, Wind Stress, and Rainfall over the Tropical Atlantic and South America. *Journal of Climate* 9(10), 2464–2479.
- Philander, S. G. (1990). *El Niño, La Niña, and the Southern Oscillation*, Volume 46 of *International Geophysics*. Academic Press.
- Phillips, O. L., L. E. O. C. Aragão, S. L. Lewis, J. B. Fisher, J. Lloyd, G. López-González, Y. Malhi, A. Monteagudo, J. Peacock, C. A. Quesada, G. van der Heijden, S. Almeida, I. Amaral, L. Arroyo, G. Aymard, T. R. Baker, O. Bánki, L. Blanc, D. Bonal, P. Brando, J. Chave, Á. C. A. de Oliveira, N. D. Cardozo, C. I. Czimczik, T. R. Feldpausch, M. A. Freitas, E. Gloor, N. Higuchi, E. Jiménez, G. Lloyd, P. Meir, C. Mendoza, A. Morel, D. A. Neill, D. Nepstad, S. Patiño, M. C. Peñuela, A. Prieto, F. Ramírez, M. Schwarz, J. Silva, M. Silveira, A. S. Thomas, H. t. Steege, J. Stropp, R. Vásquez, P. Zelazowski, E. A. Dávila, S. Andelman, A. Andrade, K.-J. Chao, T. Erwin, A. Di Fiore, E. H. C., H. Keeling, T. J. Killeen, W. F. Laurance, A. P. Cruz, N. C. A. Pitman, P. N. Vargas, H. Ramírez-Angulo, A. Rudas, R. Salamão, N. Silva, J. Terborgh, and A. Torres-Lezama (2009, 03). Drought Sensitivity of the Amazon Rainforest. *Science* 323(5919), 1344–1347.
- Ropelewski, C. F. and M. S. Halpert (1987). Global and Regional Scale Precipitation Patterns Associated with the El Niño/Southern Oscillation. *Monthly Weather Review* 115(8), 1606–1626.

- Rossow, W. B., A. W. Walker, and M. D. Roiter (1996). *International Satellite Cloud Climatology Project (ISCCP): documentation of new cloud datasets*. NASA Goddard Space Flight Center.
- Salati, E. and C. A. Nobre (1991). Possible climatic impacts of tropical deforestation. *Climatic Change* 19(1), 177–196.
- Schneider, U., A. Becker, P. Finger, A. Meyer-Christoffer, B. Rudolf, and M. Ziese (2011). GPCP Full Data Reanalysis Version 6.0 at 0.5°: Monthly Land-Surface Precipitation from Rain-Gauges built on GTS-based and Historic Data.
- Shukla, J., C. Nobre, and P. Sellers (1990). Amazon Deforestation and Climate Change. *Science* 247(4948), 1322–1325.
- Swann, A. L., M. Longo, R. G. Knox, E. Lee, and P. R. Moorcroft (2015). Future deforestation in the Amazon and consequences for South American climate. *Agricultural and Forest Meteorology* 214–215, 12 – 24.
- Taylor, K. E., R. J. Stouffer, and G. A. Meehl (2012, 2016/02/29). An Overview of CMIP5 and the Experiment Design. *Bulletin of the American Meteorological Society* 93(4), 485–498.
- Trenberth, K. E. (1997). The definition of el niño. *Bulletin of the American Meteorological Society* 78(12), 2771–2777.
- Wang, C., C. Deser, J.-Y. Yu, P. DiNezio, and A. Clement (2012). El Nino and southern oscillation (ENSO): a review. *Coral Reefs of the Eastern Pacific*, 3–19.
- Watanabe, M., T. Suzuki, R. O’ishi, Y. Komuro, S. Watanabe, S. Emori, T. Takemura, M. Chikira, T. Ogura, M. Sekiguchi, K. Takata, D. Yamazaki, T. Yokohata, T. Nozawa,

H. Hasumi, H. Tatebe, and M. Kimoto (2010, 2016/02/29). Improved Climate Simulation by MIROC5: Mean States, Variability, and Climate Sensitivity. *Journal of Climate* 23(23), 6312–6335.

Yoon, J.-H. and N. Zeng (2009). An Atlantic influence on Amazon rainfall. *Climate Dynamics* 34(2), 249–264.